ORIGINAL ARTICLE

Formability and failure response of AA5052-H32 thin sheets with friction stir spot welds during the shock tube-based impact forming

Saibal Kanchan Barik[1] · R. Ganesh Narayanan[1] · Niranjan Sahoo[1]

Abstract

In the present study, both the experimental and numerical investigations are carried out to understand the dynamic forming behavior of friction stir spot-welded (FSSW) sheet made of AA 5052-H32 sheets of 1 mm thickness using a shock tube. A hemispherical end nylon striker is propelled at high velocity to deform the FSSW sheet in biaxial mode of deformation. Furthermore, the effect of tool rotational speed and plunge speed on the FSSW joint is studied. During this analysis, a new strategy is followed to evaluate the rate-dependent flow stress–strain properties, which are incorporated during FE simulation using FE code, DEFORM-3D. Tensile test data obtained from the unwelded section of the deformed FSSW sheet is fit to Modified Johnson–Cook (MJC) model, and the rate-dependent properties are identified. In the case of the spot-welded region, a hardness-based multiplying factor is generated to evaluate the stress–strain data by fitting to MJC model. The effect of tool rotational speed and plunge speed on the welding and forming outputs are presented. Temperature evolution during FSSW is validated with the experimental data, and good correlation is obtained. The predicted material flow visualization during FSSW gives insight into the mixing of the material during the joint formation. The results agree with available findings. Various forming outputs such as effective strain distribution, necking height, and the failure pattern are predicted using MJC model in combination with Freudenthal damage model, and the results have good agreement with the experimental data.

Keywords Formability · Shock tube · FSSW · High strain rate · Failure

1 Introduction

The scarcity of global resources and environmental issues force the aerospace and automotive sectors to work on lightweight materials that can reduce the overall body weight and improve the fuel economy. Currently, the application of aluminum alloys is extensive because of their specific characteristics such as lightweight, good static and dynamic strength, better corrosion resistance, and recycling potential. However, poor welding during conventional fusion welding restricts

their applications. In the recent past, friction stir spot welding (FSSW) has been preferred to join aluminum alloy sheets in lap configuration instead of riveting or resistance spot welding because of advantages such as excellent mechanical properties, less distortion, low cost, higher energy saving, and ease of producing reliable joints consistently [1]. During the solid-state welding, heat is generated by the friction between the sheets and rotating non-consumable tool that softens the material being welded. The rotating tool stirs the softened material, and it results in inter-mixing of both the upper sheet and the lower sheet. After a certain dwell period, the tool is withdrawn, and the solid-state spot weld is formed with a pinhole at the center.

In order to produce a satisfactory friction stir spot weld, optimization of tool geometry such as the pin profile, pin, and shoulder dimensions [2], and the process parameters such as tool rotational speed, plunge speed, plunge depth, and dwell time are performed [3, 4]. The process optimization is mainly carried out to obtain acceptable mechanical strength. The effect of each process parameter on the

✉ Saibal Kanchan Barik
saibal@iitg.ac.in

R. Ganesh Narayanan
ganu@iitg.ac.in

Niranjan Sahoo
shock@iitg.ac.in

[1] Department of Mechanical Engineering, IIT Guwahati, Guwahati, Assam 781 039, India

microstructure and mechanical properties of FSSW of AA 5XXX sheets has been studied significantly. Badarinarayan et al. [2] studied the effect of tool geometry on the static strength of the spot weld. They have correlated the mechanical strength of the weld with the weld geometry, which is mainly comprised of hook height and hook width. The effect of tool rotational speed and dwell time on the joint strength is observed and reported that higher rotational speed and dwell time are preferable to achieve good mechanical and metallurgical properties [5–7]. Other researchers have observed an inverse relationship with tool rotational speed and dwell time [8]. Thus, the effect of process parameters on the quality of FSSW joint for AA 5XXX sheets is still under scrutiny.

Several mechanical tests such as lap-shear test, cross-tension test, and uniaxial tension test have been performed to understand the effect of tool and process parameters on the joint strength and extension limit at failure [4, 7–9]. Rana et al. [9] performed static mechanical tests on FSSW of AA 5052 sheets at different tool rotational speeds and reported that with the rise in rotational speed, the tensile/shear strength of the FSSW joint improves, but the cross-tension strength and the uniaxial tensile strength decrease. Similar results have been observed by Tozaki et al. [8] for the welding dissimilar Al alloys. Often static strength of the welded joints is understood. Scarce literature is found on the dynamic testing and characterization of the FSSW joints. Recently, Noh et al. [10] performed dynamic lap shear and coach-peel coupon tests to evaluate the dynamic failure behavior of the resistance spot-welded automotive steel sheets. The peak strength and the failure modes predicted by FE simulation have a good correlation with the experimental data. In the same way, the dynamic characterization of the FSSW sheets can be performed that caters to the requirements of several industrial applications.

Furthermore, the welded sheets are exposed to different loading environment in automotive and industrial applications. Thus, identification of the forming limit of the welded sheets is always important. Several investigations have been performed on the formability of Tailor Welded Blanks (TWBs) produced by different welding processes [11, 12]. Formability of the TWBs is mainly evaluated by three applications such as simple tensile test with changes in weld line orientation [13], hemispherical dome stretching test [14], and cylindrical cup drawing test [15]. Investigation on forming limit diagram (FLD) of the TWBs provided insight on the effect of different welded zones on the forming limit at different strain paths [14, 16]. Most of the studies in friction stir welding (FSW) focus on understanding the process, especially the effect of process parameters on the quality of the welds. Some focus on the formability aspects [13–15]. On the other hand, in friction stir spot weld (FSSW), only uniaxial tensile test is used to investigate the extension limit

of the welded region [9]. To the authors' knowledge, no work has been performed on the forming of sheets with FSS welds in biaxial stretching mode.

In transportation applications, strain rates in the range of 10^2 to 10^3 are often observed. Most of the studies observed that the Al alloys are rate independent at lower strain rate. However, it becomes strain rate sensitive when the rate of loading reaches a threshold limit [17]. Therefore, it is necessary to study the rate-dependent mechanical behavior of the welded sheets at different regime of strain rates. Sun and Khaleel [18] evaluated the dynamic strength of self-piercing rivets and resistance spot welds of dissimilar Al sheets using servo-hydraulic test frames with high rate actuators. They observed a decrease in displacement to failure with the increase in loading rates. Ambiz et al. [19] studied the tensile properties and fracture behavior of aluminum FSW sheets at a constant speed of 10 m/s, and found that like base material, the ductility of the welded joint increased at higher strain rate. There is no literature available on the effect of dynamic loading on FSSW joint. Thus, in the present study, it is decided to investigate the dynamic behavior of aluminum sheets with FS spot welds in shock tube-based impact loading environment.

In recent past, shock tube has been utilized to generate dynamic loading for a short duration [20–23]. The shock tube generates a shock wave after bursting a diaphragm, which separates high-pressure driver section and low pressure-driven section of the shock tube. The high pressure–induced gas driven by the high-velocity shock wave creates a dynamic loading environment, which has been utilized in many studies to understand the dynamic behavior of the material [20, 22, 24–26]. Barik et al. [26] used the shock wave to drive a hemispherical end nylon striker, which imparts the specimen kept at the end of the shock tube at a high velocity. The same experimental setup can also be used to understand the biaxial dynamic forming behavior of the welded sheets.

Generally, in sheet metal forming processes, the blank is typically made of one piece. Thus, in the last decade, research on the forming behavior of the welded sheet increased significantly [13, 19]. Scarce attempts are made to understand the effect of welding parameters during dynamic forming of the welded sheet. Furthermore, the shock tube has not been used in this context. Thus, the present study focuses on the investigation of the dynamic forming behavior of the FSSW joints made from a pair of 1 mm thick AA 5052-H32 sheets. The effect of tool rotational speed and plunge speed on the welded sheet is understood during the shock tube-based impact forming. In addition to it, DEFORM-3D FE code is used to carry out FE simulation of the FSSW. The simulated welded sheet is further considered for high-velocity forming simulation to retrieve its material performance during forming. In the current analysis, the temperature evolution data obtained from FSSW experiment

Table 1 Tensile properties of AA 5052-H32 base sheet

Temperature (°C)	RT	100	200	300	400
σ_{ys} (MPa)	171	167	168	161	158
σ_u (MPa)	238	235	221	203	173
n	0.143	0.126	0.115	0.095	0.049
K (MPa)	348	321	292	257.3	212
ε_u (%)	8.7	10.1	9.8	6.3	3.6
ε_t (%)	9.6	12.3	10.4	11.3	11.9

σ_{ys} yield strength, σ_u ultimate tensile strength, n strain hardening coefficient, K strength coefficient, ε_u uniform elongation, ε_t total elongation, gauge length 50 mm, *RT* room temperature

are validated with FE simulation. The material flow is also predicted by FE simulation in order to obtain insight on the joint formation. Apart from welding, various forming outputs such as dome height, effective strain distribution, and fracture pattern obtained from experiments are validated with FE simulation results.

2 Experimental details

2.1 FSSW experiments

FSSW experiments are performed on a pair of 1 mm thick AA 5052-H32 sheets. The chemical composition of the base sheets includes Mg %: 2.64, Cu %: 0.11, Si %: 0.95, Fe %: 0.28, Mn %: 0.14, Cr %: 0.33. The mechanical properties of the sheet along the 0° to the rolling direction (RD) are evaluated by uniaxial tensile tests at room temperature and at

elevated temperatures in UTM at a crosshead speed of 1 mm/min. The true stress–strain data at elevated temperatures are fit to Hollomon flow model and the material constants are identified (Table 1). The true stress–strain curves at different temperatures are illustrated in Fig. 1. The plastic strain ratios (*r*) of the material are obtained at room temperature as per ASTM E-517. *r* value along 0°, 45°, and 90° w.r.t. rolling direction are 0.73, 0.85, and 0.85 respectively.

In this study, a tool made of H13 tool steel with a flat shoulder and a straight cylindrical pin is selected to fabricate FSSW joints. The tool shoulder diameter, pin diameter, and pin height are 18 mm, 6 mm, and 1.2 mm respectively. FSSW experiments are performed at three different rotational speeds, 750 rpm, 900 rpm, and 1200 rpm, and two different plunge speeds, 7.5 mm/min and 10 mm/min, to understand their effect on the weld strength during high-velocity shock tube-based forming experiments. The plunge depth is kept constant as 1.6 mm. The dwell time of 10 s is maintained based on the existing literature [27] to have better welding properties. All the experiments are carried out thrice for repeatability. Out of these, two welded samples are considered for shock tube-based forming experiments, and one sample is kept for weld characterization.

During FSSW experiments, the evolution of temperature is measured by mounting K- type thermocouple on the surface of the specimen at a distance of 10 mm from the shoulder edge (Fig. 2). The head of the thermocouple is properly adhered to the specimen by a thermal insulator to avoid heat loss to the environment during the experiment. The output from the thermocouple is connected to a DAQ unit (Make: Agilent; Model: 34970a) for data recording and visualization.
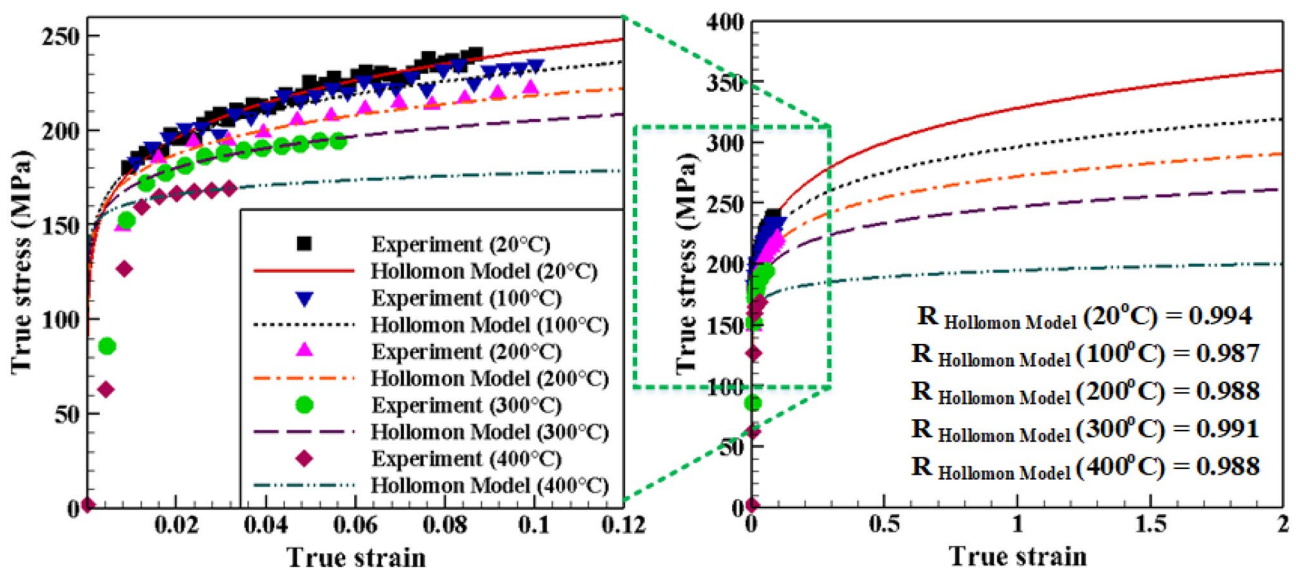
Fig. 1 True stress–strain curves obtained from Hollomon flow stress model at different elevated temperatures
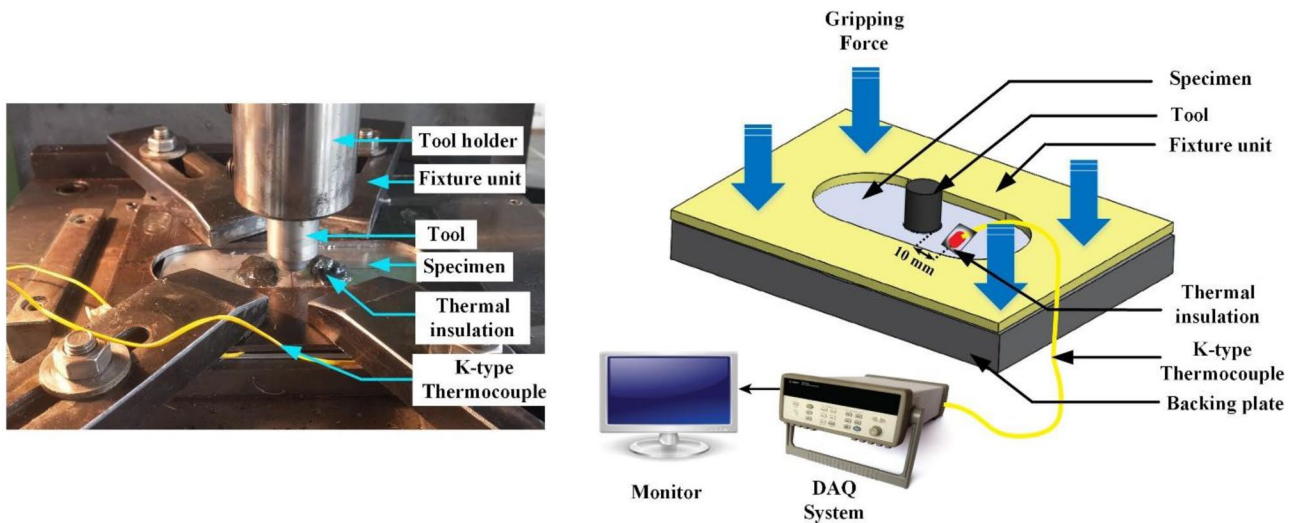
Fig. 2 Thermocouple mounted on the specimen to measure temperature evolution during FSSW experiments

2.2 Shock tube-based impact forming experiment

In the present study, a shock tube facility has been utilized to deform the FSS welded sheet at high strain rates (Fig. 3). The details of the experimental setup are described elsewhere [26, 28]. A nylon striker of diameter 54.8 mm and 95 mm overall length with a hemispherical end is kept at a distance of 300 mm from the end of the shock tube (Fig. 3). When the diaphragm bursts, the shock wave propels the striker at a high velocity, and it hits the specimen mounted at the end of the shock tube. The pressure developed at the closed end of the shock tube due to the rapid motion of the striker is removed from the pressure outlet. A set of IR sensors are mounted at a distance of 130 mm from the end of the shock tube to measure the velocity of the striker. During the analysis, bursting pressure in the driver section is kept constant at 15.05 ± 0.35 bar for all the cases of forming. The pressure–time graph recorded by two pressure transducers (P_1 and P_2) during the experiment is shown in Fig. 4. The experimental condition generates an average incident pressure of 3.41 ± 0.17 bar, reflected pressure of 11.63 ± 0.21 bar, and striker velocity of 68.55 ± 0.76 m/s.

In order to measure effective strain ($\bar{\varepsilon}$) generated on the FSS welded sheet after the shock tube-based impact experiment, circular grids of average diameter 1.83 ± 0.03 mm are printed on the top sheet by chemical etching method. The circular grids deformed into elliptical grids after deformation. The major and minor diameters of the elliptical grids are measured and the effective strain is calculated by using Hill's 1948 yield function.
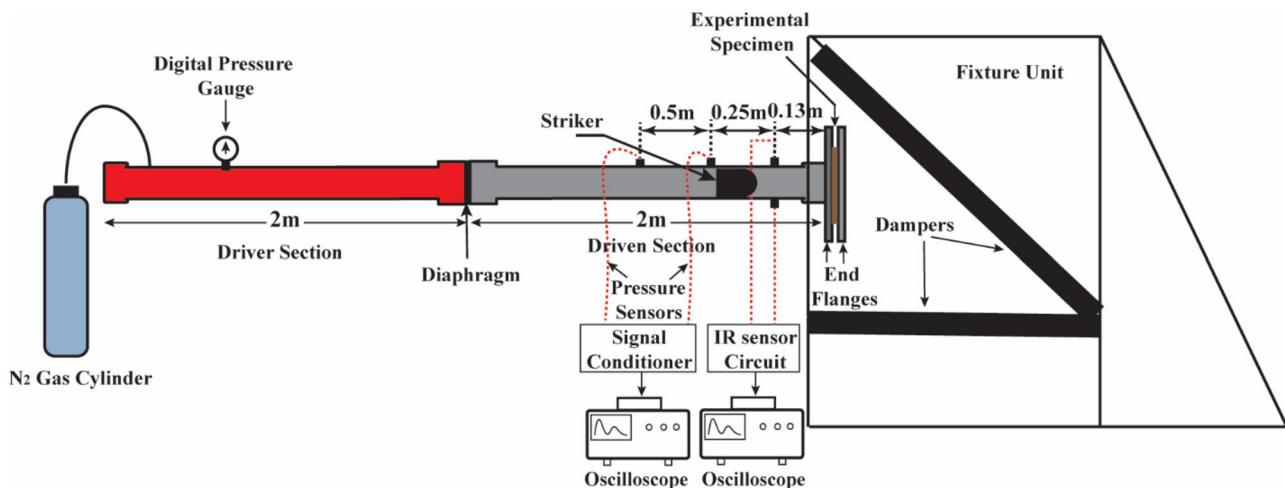

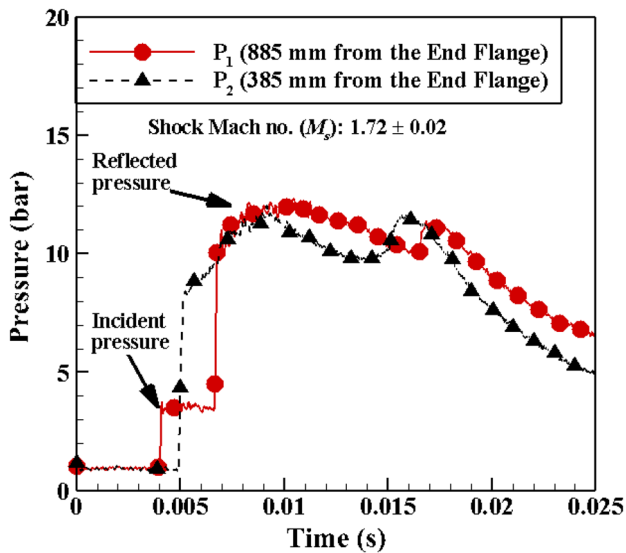**Fig. 3** Schematic representation of the shock tube experimental facility

Fig. 4 Pressure–time graph obtained for bursting pressure 15.05 ± 0.35 bar

The details about Hill's 1948 yield function are discussed in Sect. 3.2.1.

3 Numerical simulation of shock tube-based forming of FSSW sheet

The complete process (FSSW + Forming) is modeled in three stages in the multi-operation layout of DEFORM-3D FE code (Fig. 5). The plunging and dwelling operation in FSSW is modeled in two stages as a thermo-mechanical problem, and the welded sheet is redirected for high-velocity biaxial forming in the third stage. The multi-operation layout establishes an interactive setup among all the stages of simulation in such a way that the material properties and boundary conditions of an object can be easily passed between two successive operations. Therefore, the material properties of the sheets after welding are easily retrieved before the start of the FE simulation of the forming process. The dimensions of all the parts of the model are same as per the experiments. The workpiece is modeled as a deformable plastic body, whereas the welding tool, end flanges, and the striker are modeled as a rigid body (Fig. 5). The detailed procedures of the FE simulation are discussed below.

3.1 FE simulation of FSSW

3.1.1 Geometric modelling and mesh generation

The complete FSSW operation is solved in two stages as a fully coupled 3-dimensional thermo-mechanical problem, which is solved by Lagrangian implicit method. The workpiece is

considered a deformable plastic material, and it is modeled as a single block, i.e., the two sheets are modeled as a unique simulation object for which the zone corresponding to the shoulder position during welding is presented with material continuity (Fig. 6). This choice was made in order to avoid contact instabilities during material bonding, and at the same time, taking to account the thermal barrier between the interface of the sheets [29].

During this analysis, coupled tetrahedral meshing has been defined for the workpiece. To improve the computational efficiency of the model, biased meshing is used at the interaction zone of the workpiece and the tool using mesh density window (Fig. 6). To understand the effect of element size, several mesh sizes such as 0.7 mm, 0.5 mm, and 0.3 mm are selected, whereas the rest of the workpiece domain is meshed with minimum element size of 1 mm with a size ratio of 2. The mesh independency analysis is performed for a welding condition with rotational speed 750 rpm, and plunge speed 7.5 mm/min. The peak temperature recorded by a thermocouple at a distance 10 mm from the shoulder edge is compared with the FE simulation results. Though the results obtained for element sizes 0.5 mm and 0.3 mm do not vary much and have a good agreement with the experiment, the computational time for 0.3 mm element size increases significantly. Thus, 0.5 mm element size inside the mesh density window is considered for simulating FSSW. Along with this, the maximum effective strain and effective strain rate are also compared for various element sizes (Table 2). The elements corresponding to 0.5 mm and 0.3 mm predict almost the same values. Hence, selecting 0.5 mm element size is justified. Since the yield strength of tool material (H13 tool steel) is much higher than AA 5052-H32 workpiece, the assumption of choosing the tool as a rigid body is valid. In the analysis, the tool is also meshed with tetrahedral element of 0.5 mm size to define a precise geometry, which generates 37,160 number of elements.

3.1.2 Material model for FSSW simulation

During FSSW process, the material undergoes large plastic deformation at high temperature. Thus, the high-temperature tensile test data of AA 5052-H32 sheet (Fig. 1) are fit to Hollomon equation ($\sigma = K\varepsilon^n$), and the material constants are identified (Table 1). Those material constants are again utilized to extrapolate the flow stress for larger strain value and incorporated during FE simulation as tabular data. The other temperature-dependent material properties considered during FE simulation are obtained from literature [30], and also mentioned in Table 3. The thermo-mechanical properties of H13 tool steel are obtained from the material library database of DEFORM-3D [31].

3.1.3 Boundary and frictional contact conditions

The tool and the workpiece are defined with boundary conditions in such a way that the actual physical phenomenon
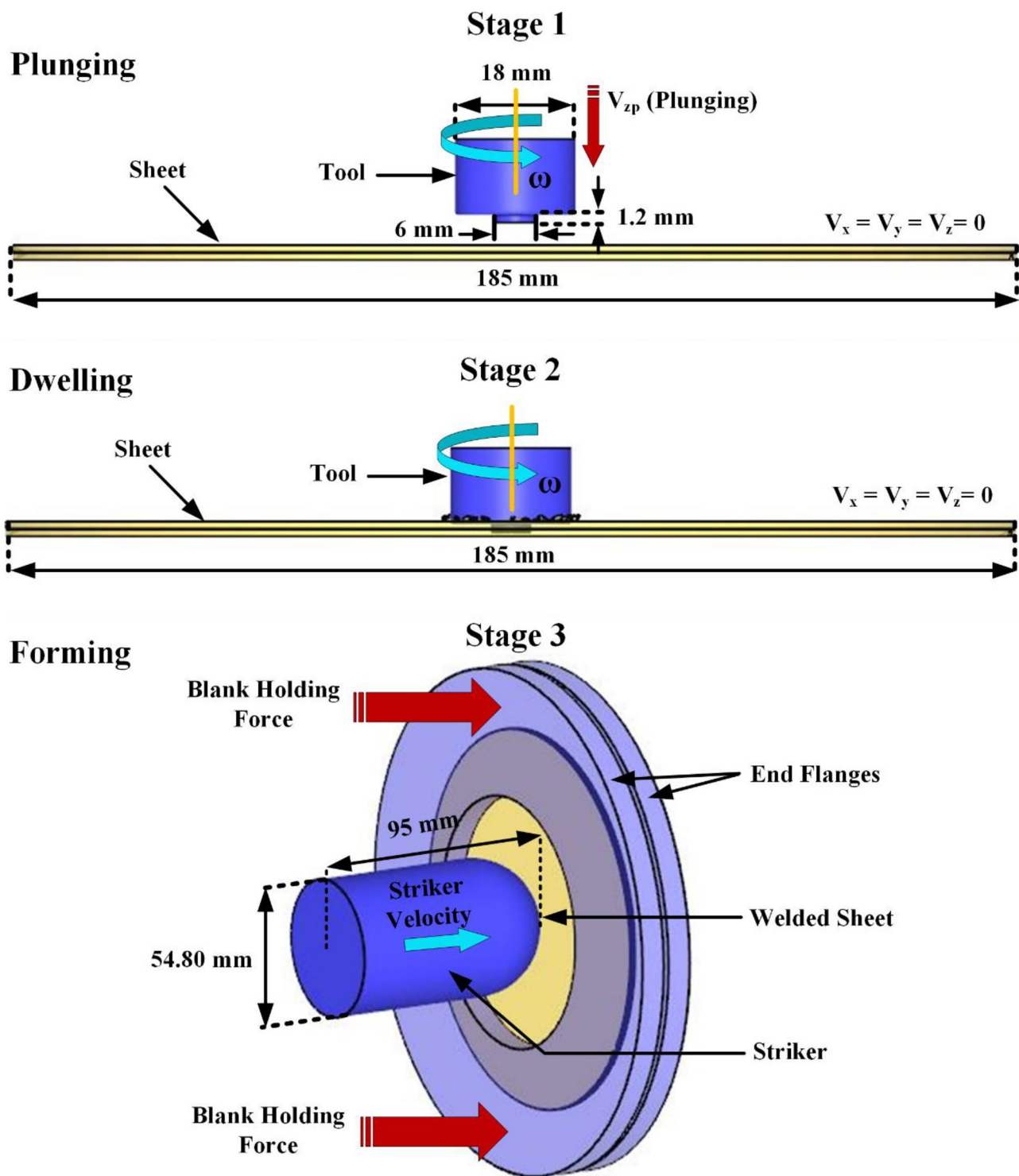
Fig. 5 Stages of FE simulation for shock tube-based forming of FSS welded sheet

during FSSW can be accurately simulated. The boundary conditions defined during modelling are depicted in Fig. 6. The motion of the side faces of the workpiece is constrained in X, Y, and Z directions, while the motion of the bottom face of the workpiece is only restricted in Z-direction. The

plunge speed and the rotational speed of the tool are defined along the negative Z-axis as per the experiment.

The initial temperature of the workpiece and the tool are set as 25 °C. The heat transfer between the workpiece/tool surface and the environment can be expressed by Eq.
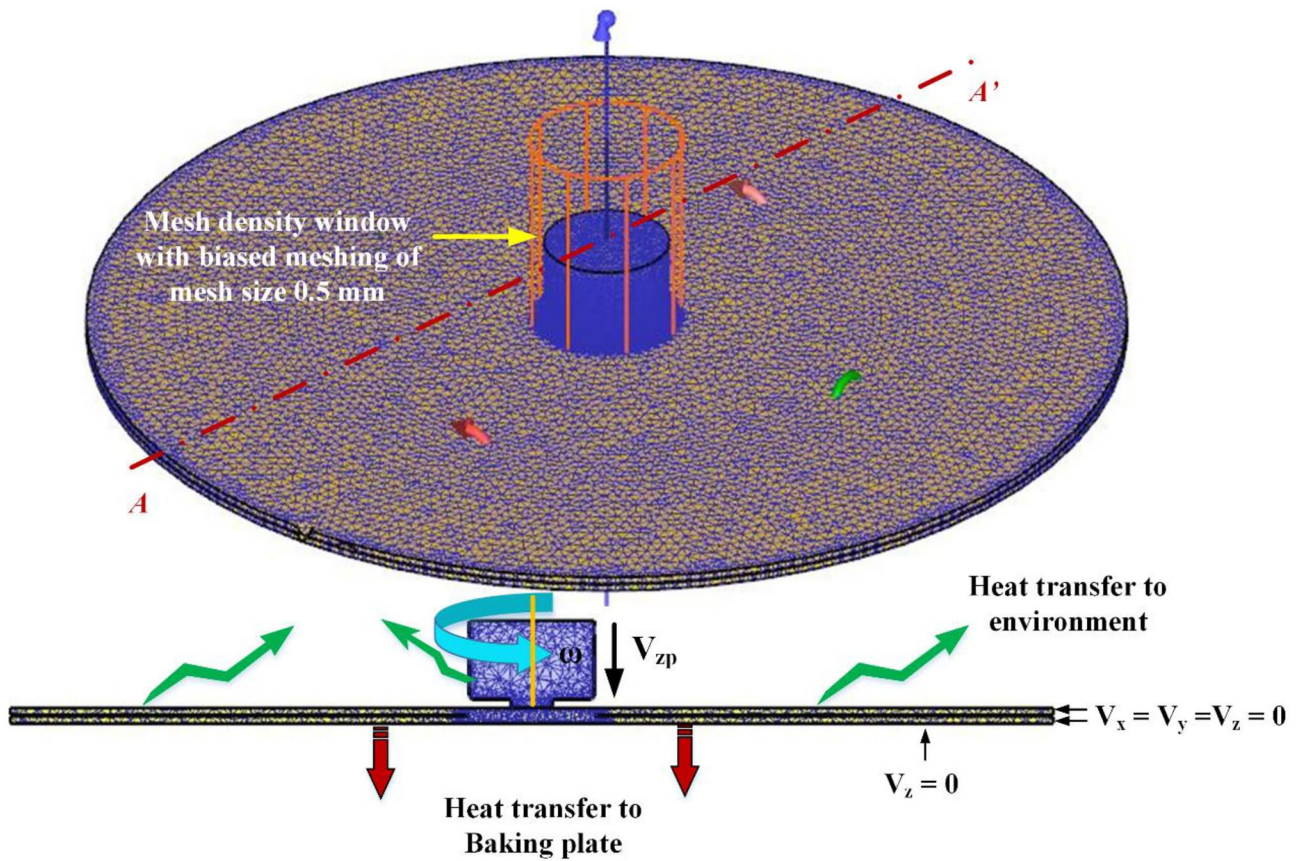
Fig. 6 Meshed assembly of the model with boundary conditions

(1). Furthermore, the heat exchange at the interaction region between the tool, sheet, and baking plate can be defined by Eq. (2)

$$-K\frac{\partial T}{\partial n} = \sigma_b \varepsilon_b \left(T^4 - T_b^4\right) + h_a\left(T - T_b\right) (n \text{ is the direction vector})$$
(1)

$$-K\frac{\partial T}{\partial Z} = h_b\left(T - T_b\right)$$
(2)

where σ_b is the Stefan-Boltzmann constant, ε_b is the emissivity of the material, K is the thermal conductivity of the material, T_b is the ambient temperature, h_a is convective heat transfer between workpiece/tool and the environment, and h_b is the convective heat transfer coefficient between the workpiece and the backing

plate. To improve the computational efficiency of the FE simulation, the backing plate is replaced by a local heat exchange window to define the heat transfer between the bottom face of the sheet and the environment with the convention coefficient (h_b) as 500 W/m^2°C [31] as shown in Fig. 6. The heat exchange from the other faces of the workpiece and the tool to the environment are also defined by generating heat exchange local windows with convection coefficient (h_a) as 20 W/m^2°C. The emissivity for AA 5052-H32 sheets and H13 tool is considered 0.03 and 0.7, respectively [31]. It has been observed that the heat transfer between the tool and the workpiece is higher than the workpiece and the environment. Thus, the heat transfer coefficient between them is considered 11,000 W/m^2°C [29].

Table 2 Mesh sensitive analysis for FSSW stage

Element size (mesh density window)	Number of elements	Peak temperature (10 offset to shoulder) (°C)	Maximum effective strain	Maximum effective strain rate (s^{-1})	Computational time (*min*)
Experiment	–	257.26	–	–	–
0.7 mm	63,852	277.36	148	68.36	3120
0.5 mm	132,914	268.42	104	52.34	4745
0.3 mm	218,652	267.12	101	52.92	9023

Table 3 Temperature-dependent mechanical properties of AA5052 [30] and H13 tool steel [31]

Temp. (°C)	ρ (Kg/m³)	E (GPa)	K_p (W/m °C)	α (µ/°C)	C (N/mm²/°C)	υ
AA5052-H32						
20	2781.25	72	162.5	21	2.43	0.33
80	2756.25	68	168.75	24	2.43	0.33
180	2695	64	193.75	25	2.43	0.33
280	2650.5	56	206.25	26	2.43	0.33
380	2610.66	40	225	27	2.43	0.33
480	2605	22	237.5	28.5	2.43	0.33
H13 tool steel						
20	7780	210.29	24.57	11.7	2.78	0.3

ρ density, C heat capacity, K_p thermal conductivity, α coefficient of thermal expansion, E Young's modulus, υ Poisson's ratio

The contact condition between the workpiece and the tool during FE simulation of FSW is complex. In few studies, sliding frictional condition is defined, while in most of the studies, sticking friction model (Eq. 3) is best suited during simulation of the material state during FSW.

$$\tau = mk \tag{3}$$

where τ and k are the frictional stress, and the shear yield stress of the material, respectively. m represents the shear friction factor. In order to calibrate the correct magnitude of m, several numerical simulations were performed with different m values for a weld condition with 750 rpm and 7.5 mm/min plunge speed, and the peak temperature at a distance of 10 mm from the shoulder edge are compared with the experimental result (Fig. 7). For simulation, the optimum element size of 0.5 mm in the weld spot was considered. The result represents a good correlation of
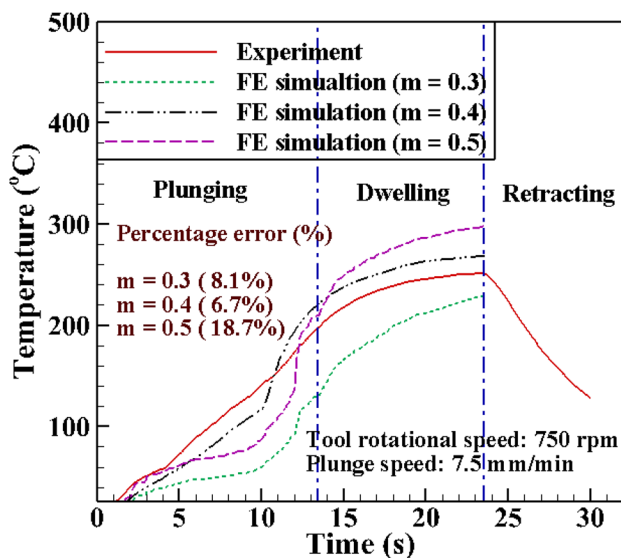

Fig. 7 Comparison of temperature evolution during FE simulation with experiment for various m values

FE simulation with the experiment for $m = 0.4$, with 6.7% deviation. Thus, the value of $m = 4$ is considered a constant for other cases of FE simulation.

3.2 FE simulation of shock tube-based forming

3.2.1 Material model for forming operation

After completion of FSSW simulation, the workpiece is redirected for high strain rate forming in DEFORM-3D. The multi-operation environment allows to transfer object data between two successive operations, which helps to retrieve all the welding properties of the workpiece before the start of the forming simulation. The shock tube-based forming takes place at the atmospheric temperature under high strain rate condition. Thus, incorporation of the rate-dependent mechanical properties to the sheet with FSSW is crucial. For an accurate prediction of the forming behavior of the welded sheet, it is unfair to assign the mechanical properties of the base material to both the spot weld and unwelded sections of the sheet. Therefore, a new strategy is followed during this analysis, in which the single block welded workpiece is separated into two zones such as spot weld zone and unwelded zone (Fig. 8). Both the zones are assigned with the rate-dependent mechanical properties separately obtained from experiments.

In most of the research work, Split Hopkinson Pressure Bar (SHPB) is utilized to conduct tensile test at high strain rate. In this current work, a new method is followed to identify the rate-dependent mechanical properties of the spot weld and unwelded region. For the unwelded section, a tensile sample is cut in a safe location of the deformed sheet near to the fracture after the shock tube-based forming experiment (Fig. 8a). The tensile test is performed on the bent tensile sample without any post-treatment at a crosshead speed of 1 mm/min in UTM. On the other hand, sectioning the tensile sample from the FS spot weld of the deformed sheet is impossible because of the presence
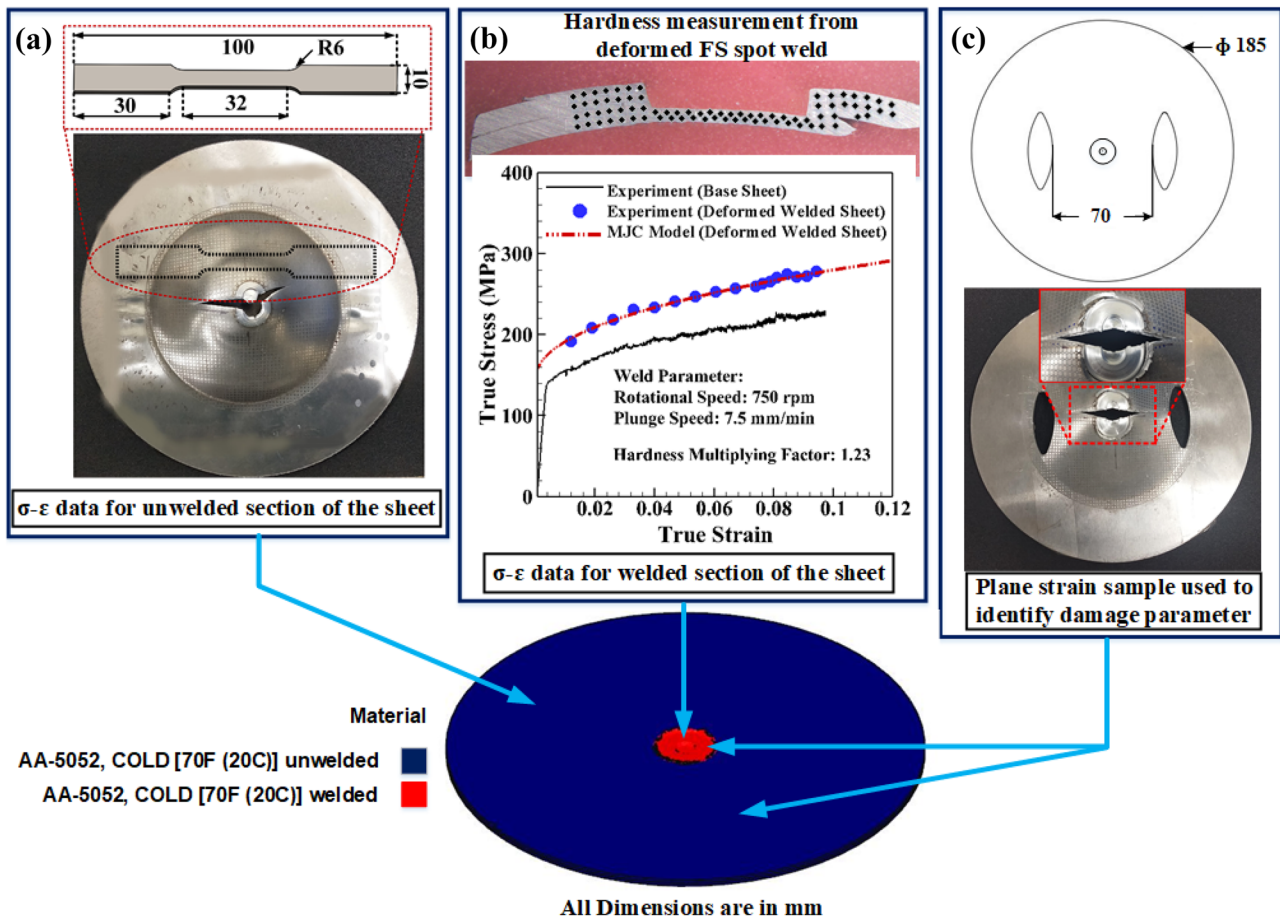
Fig. 8 Procedure to define material constants during FE simulation of shock tube-based forming of FSSW sheets [(**a**) corresponds to identification of σ - ε data for the unwelded section of the sheet (**b**) corresponds to identification of σ - ε data for the welded section of the sheet, and (**c**) corresponds to identification of the damage parameters for both the welded and unwelded section of the sheet]

of fracture. Thus, the rate-dependent plastic behavior of the spot weld of the sheet is correlated with the hardness variation in the weld spot after forming. A hardness increment factor has been identified between the average hardness value of the welded joint after forming to the undeformed base sheet, and that factor is multiplied to the true stress–strain data of the undeformed base sheet to obtain the rate-dependent stress–strain curve for the FS spot weld (Fig. 8b). The experimentally identified stress–strain data of the spot weld and unwelded sections of the sheet is fit to modified Johnson–Cook (MJC) model given in Eq. (4), and the material constants are identified.

$$
bar\sigma = [A + B(\bar{\varepsilon})^n] \times \left[1 + C_1 \ln \frac{\dot{\bar{\varepsilon}}}{\dot{\bar{\varepsilon}}_0} + C_2 \left(\ln \frac{\dot{\bar{\varepsilon}}}{\dot{\bar{\varepsilon}}_0} \right)^2 \right] \quad (4)
$$

where A, B, and n are the material constants that are identified at a reference strain rate ($\dot{\bar{\varepsilon}}_0$), which is kept as one [32, 33], C_1 and C_2 are the strain rate sensitivity constants, $\dot{\bar{\varepsilon}}$ is the real strain rate. During high-velocity shock tube experiment, it is practically difficult to identify the real strain rate

because of the restrictions in instrumentation. However, it is required while using Eq. (4). Thus, FE simulation is carried out to obtain the average strain rate near the pole region of the welded sheet. For this modelling, the rate-dependent true stress–strain data of both the welded and unwelded section are fit to Hollomon hardening model ($\bar{\sigma} = K\bar{\varepsilon}^n$), and the material constants (K and n) are identified (Table 4). The material constants are further utilized to calculate flow stress for larger strain (Fig. 9), and the stress–strain data are incorporated in a tabular form during FE simulation. The average strain rates during the forming of different welded sheets are mentioned in Table 4. Furthermore, the identified strain rates are again utilized in MJC model to calculate the rate-dependent material constants mentioned above for FSSW and unwelded sections of the sheet by the curve fitting method (Fig. 9). During the curve fitting, the lower range and the upper range of the MJC model material constants are identified from the literature [32–34], and the best fit values as mentioned in Table 4 are further utilized for the calculation of the flow stress for larger strain (Fig. 9).

Defining material anisotropy is essential for an accurate prediction of formability. During the prediction of the plastic

deformation of any material, flow stress model, yield function, and flow rule are required. In this study, it is assumed that AA 5052-H32 sheet would follow Hill's 1948 yield criterion (Eq. 5) [35] and the associated flow rule.

$$F(\sigma_{22} - \sigma_{33})^2 + G(\sigma_{33} - \sigma_{11})^2 + H(\sigma_{11} - \sigma_{22})^2 + 2L\sigma_{23}^2 + 2M\sigma_{31}^2 + 2N\sigma_{12}^2 = 2f(\sigma_{ij}) \tag{5}$$

where f is the yield function; σ_{ij} denotes the stress components; F, G, H, L, M, and N are the material constants, which are calculated from r_0, r_{45} and r_{90} (enlisted in Sect. 2.1).

The effective strain ($\bar{\varepsilon}$) is calculated by the relation [35]

$$\bar{\varepsilon}^2 = \frac{G + H}{(FG + FH + GH)^2} \left[F^2(G + H)\varepsilon_1^2 + G^2(F + H)\varepsilon_2^2 + H^2(F + G)\varepsilon_3^2 \right] \tag{6}$$

It is observed that the failure pattern is sensitive to the flow stress model, fracture model, coefficient of friction (μ), and angle of contact (θ) between the sheet and the striker. Along with the best feasible material models, the Coulomb's coefficient of friction (μ) is also optimized, which is defined as the contact condition between the striker and the workpiece during plastic deformation. μ is varied between 0.005 and 0.2 to obtain an acceptable failure pattern similar to the experiment. At $\mu = 0.2$, the material fails, and complete plug ejection was observed, whereas the failure pattern is unreal at $\mu = 0.005$. After several trials, $\mu = 0.05$ resulted in an acceptable failure pattern and has a good agreement with the experiment. Thus, $\mu = 0.05$ is kept constant for further cases of forming simulation. In order to avoid sliding between the end flanges and the sheet, $\mu = 0.1$ has been assumed.

3.2.2 Identification of damage parameter during forming

Severe plastic deformation above a critical limit leads to the onset of necking and initiation of crack. During this study, Freudenthal failure model (Eq. 7) is utilized to understand

Table 4 Identification of material constants for Hollomon model and MJC model

Hardening model		Strain rate (s^{-1})	Hardness multiplying factor in case of FSSW	Hollomon Model		MJC Model				
Material constants				K (MPa)	n_1	A (MPa)	B (MPa)	n_2	C_1	C_2
FS spot weld	**R.S: 750 rpm P.S: 7.5 mm/min**	2356	1.23	417.76	0.18	151.2	408.4	0.45	−0.0793	0.0094
	R.S: 750 rpm P.S: 10 mm/min	2373	1.28	437.38	0.18	145.3	475.5	0.43	−0.0845	0.0095
	R.S: 900 rpm P.S: 7.5 mm/min	2288	1.36	463.77	0.18	148.8	404.7	0.44	−0.0704	0.0102
	R.S: 900 rpm P.S: 10 mm/min	2315	1.31	446.75	0.18	141.2	388.7	0.43	−0.0895	0.0122
	R.S: 1200 rpm P.S: 7.5 mm/min	2415	1.41	478.18	0.18	153.3	409.9	0.47	−0.0471	0.0078
	R.S: 1200 rpm P.S: 10 mm/min	2386	1.38	470.61	0.18	146.5	398.5	0.45	−0.0662	0.0103
Unwelded region	**R.S: 750 rpm P.S: 7.5 mm/min**	2356	–	438.98	0.22	132.7	462.9	0.47	−0.1621	0.0196
	R.S: 750 rpm P.S: 10 mm/min	2373	–	465.87	0.25	136.2	616.9	0.45	−0.0961	0.0082
	R.S: 900 rpm P.S: 7.5 mm/min	2288	–	423.13	0.21	138.6	457.5	0.45	−0.0912	0.0095
	R.S: 900 rpm P.S: 10 mm/min	2315	–	425.47	0.21	146.6	429.8	0.45	−0.0824	0.0088
	R.S: 1200 rpm P.S: 7.5 mm/min	2415	–	419.81	0.22	143.3	386.6	0.42	−0.0868	0.0088
	R.S: 1200 rpm P.S: 10 mm/min	2386	–	451.63	0.24	136.6	519.5	0.44	−0.0912	0.0087

R.S rotational speed, *P.S* plunge speed
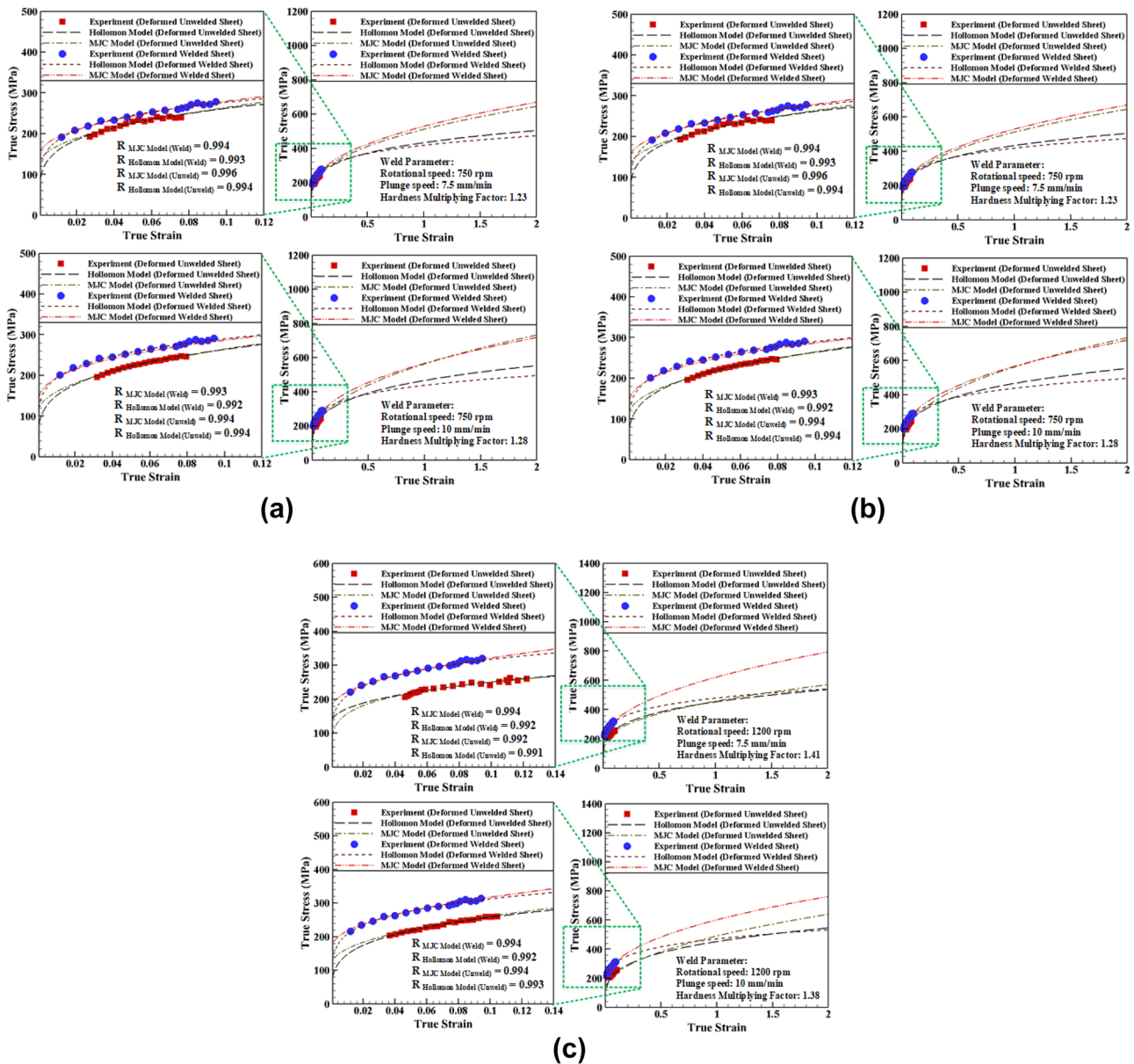
Fig. 9 Identification of rate-dependent material parameters by curve fitting method for FS spot weld and unwelded section of the sheets [**a** corresponds to rotational speed: 750 rpm, plunge speed: 7.5 mm/min and 10 mm/min; **b** corresponds to rotational speed: 900 rpm, plunge speed: 7.5 mm/min and 10 mm/min; **c** corresponds to rotational speed: 1200 rpm, plunge speed: 7.5 mm/min and 10 mm/min]

the occurrence of ductile fracture and propagation of crack on AA 5052-H32 sheets with FS spot welds during shock tube-based impact forming.

$$\int_{0}^{\varepsilon_f} \bar{\sigma} d\bar{\varepsilon} = F_1 \tag{7}$$

where $\bar{\sigma}$ is the effective stress, $\bar{\varepsilon}$ is the effective strain, ε_f is the failure strain, and F_1 is the critical damage parameter. Several failure models are available in DEFORM-3D data

base [31]. However, Freudenthal model is chosen in this study because of its better accuracy in predicting the failure pattern and fracture strain during shock tube sheet forming as observed elsewhere [26]. In the current work, circle grids of grid diameter 1.5 mm are generated on the surface of the workpiece before the start of the forming simulation (Fig. 10a). The strain paths at a location near to the failure of the deformed FS spot-welded sheets are predicted (Fig. 10b). It is observed that the sheet stretches biaxially at the initial stage, and when the critical damage parameter is reached,

necking initiates, and the strain path shifts towards the plane strain condition (Fig. 10b). Thus, by assuming plane strain condition ($\varepsilon_2 = 0$) during the deformation the critical damage parameter for Freudenthal model is calculated. The stress ratio and strain ratio required for the calculation of critical damage parameter (F_1) can be derived from Hill's 1948 yield criterion assuming no planar anisotropy condition, i.e. $r = r_0 = r_{45} = r_{90} = 0.73$, and plane strain condition (refer Appendix) and mentioned in Eq. (8).

$$\frac{\sigma_1}{\bar{\sigma}} = \frac{d\bar{\varepsilon}}{d\varepsilon_1} = \sqrt{\frac{2(2+r)(1+r)}{3(1+2r)}} \qquad (8)$$

where σ_1 is the maximum principal stress, and $\varepsilon_1 = \varepsilon_f$ is the failure strain in-plane strain deformation. The failure strain, $\varepsilon_f = 0.34$ is identified by deforming a plane strain sample of diameter 185 mm in the shock tube experiment (Fig. 8c). The critical damage parameter for Freudenthal damage model is calculated for both the FS spot weld and unwelded sections of the sheet as listed in Table 5 and incorporated during FE simulation during the forming stage. Other material properties are enlisted in Table 6.

3.2.3 Mesh details and mesh sensitive analysis for forming of sheets with FS spot welds

A new mesh window is generated on the deforming zone of the welded sheet. To optimize the mesh density and computational time, the welded sheet has meshed with a constant element size ratio of 6, which represents the ratio of the largest element edge to the smallest element edge. The largest element size inside the mesh window is decided as 1. However, the minimum element size for this analysis is finalized by mesh sensitivity analysis. Various element sizes such as 1 mm, 0.5 mm, 0.33 mm, 0.25 mm, and 0.2 mm are considered for the analysis. The mesh independency analysis is carried out for forming the sheet with spot weld at the welding condition, 750 rpm, and 7.5 mm/min plunge speed. During this analysis, Hollomon hardening model is used along with Freudenthal failure model. The material constants for the models can be found in Tables 4 and 5. The effective strain ($\bar{\varepsilon}$) distribution obtained from FE simulations using different element sizes are compared with experimental data as depicted in Fig. 11. The results illustrate a good agreement between experiments and simulation results with element sizes, 0.25 mm and 0.2 mm. However, due to the significant
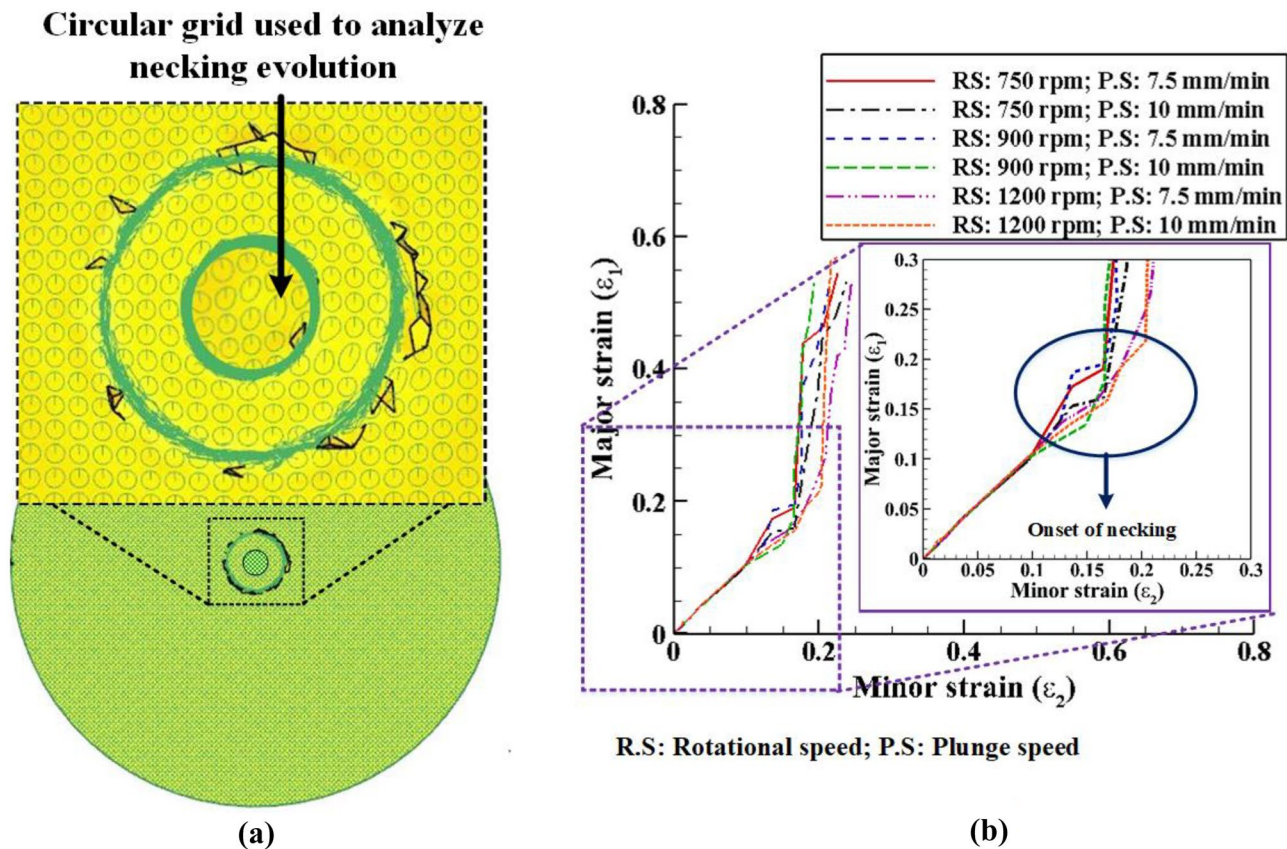
Fig. 10 (**a**) Necking evolution analysis using circular grid method (**b**) Strain path evolution during shock tube based forming of sheets with FSSW

Table 5 Critical damage parameter for Freudenthal failure model

Welding condition		Critical damage parameter (MPa)
FS spot weld region	R.S: 750 rpm P.S: 7.5 mm/min	98.51
	R.S: 750 rpm P.S: 10 mm/min	103.12
	R.S: 900 rpm P.S: 7.5 mm/min	107.68
	R.S: 900 rpm P.S: 10 mm/min	105.34
	R.S: 1200 rpm P.S: 7.5 mm/min	115.33
	R.S: 1200 rpm P.S: 10 mm/min	111.36
Unwelded region	R.S: 750 rpm P.S: 7.5 mm/min	86.68
	R.S: 750 rpm P.S: 10 mm/min	87.54
	R.S: 900 rpm P.S: 7.5 mm/min	88.76
	R.S: 900 rpm P.S: 10 mm/min	89.42
	R.S: 1200 rpm P.S: 7.5 mm/min	87.66
	R.S: 1200 rpm P.S: 10 mm/min	87.12

increase in computational time for 0.2 mm element size, the FE simulations of all the forming cases are carried out with the minimum element size 0.25 mm.

4 Results and discussion

4.1 Temperature evolution during FSSW experiments

The temperature signals measured at a distance of 10 mm from the shoulder edge during FSSW experiments are compared with FE simulation, and the results have a good agreement in all the welding conditions (Fig. 12). The rise in temperature is directly proportional to the rotational speeds, and the effect is predicted correctly by FE simulations. The effect of plunge speed during FSSW is also analyzed by FE simulation. It is observed that the decrease in plunge speed increases the temperature. However, the effect is insignificant. A maximum deviation of about 8.67% is observed between simulation and experimental data for the case with 1200 rpm and 7.5 mm/min. For all other cases, the predictions are acceptable.

The temperature evolution during plunging and dwelling stages is well captured by FE simulation. During plunging, the temperature increases monotonically because of the increase in contact between the tool and the workpiece. The temperature rise during plunging is largely dependent on the plunge speed. The temperature rise is faster in the case of 1200 rpm (Fig. 12). The temperature rise continues further during the dwelling period, and the rate at which temperature increases is directly proportional to the rotational speed (Fig. 12). The rate of temperature rise with the increase in plunge speed is not so significant. The peak temperature during welding is always captured just before the tool retraction. The temperature distribution along the transverse direction of the weld spot at the interference of two sheets ($z = 1$ mm) is illustrated in Fig. 13. The temperature distribution profile matches well with the results available in the existing literature [36].

4.2 FSSW joint characterization: stir zone prediction and hook morphology evaluation

After FSSW, the joint is divided into three zones namely stir zone (SZ), thermo-mechanically affected zone (TMAZ), and heat-affected zone (HAZ) based on microstructure. The severe plastic deformation at elevated temperature in SZ develops finer grains due to dynamic recrystallization. The SZ is surrounded by TMAZ, which experiences less heat input and plastic deformation than SZ, whereas the HAZ experiences a thermal cycle without plastic deformation. The microstructure evolved at different zones is illustrated in Fig. 14.

Table 6 Properties incorporated during FE simulations of forming

| Properties	Value
Mass density of AA 5052-H32 sheet (kg/m^3) at room temperature	Refer Table 3
Mass density of nylon (kg/m^3)	1140
Young's modulus of AA 5052-H32 sheet (MPa)	Refer Table 3
Young's modulus of nylon (MPa)	3810
Coulomb's coefficient of friction between striker and sheet	0.05
Coulomb's coefficient of friction between end flanges and sheet	0.1
Rate-dependent $\sigma - \varepsilon$ data of AA5052-H32 unwelded sheet	Refer Fig. 9
Rate-dependent $\sigma - \varepsilon$ data of AA5052-H32 FS spot-welded sheet	Refer Fig. 9
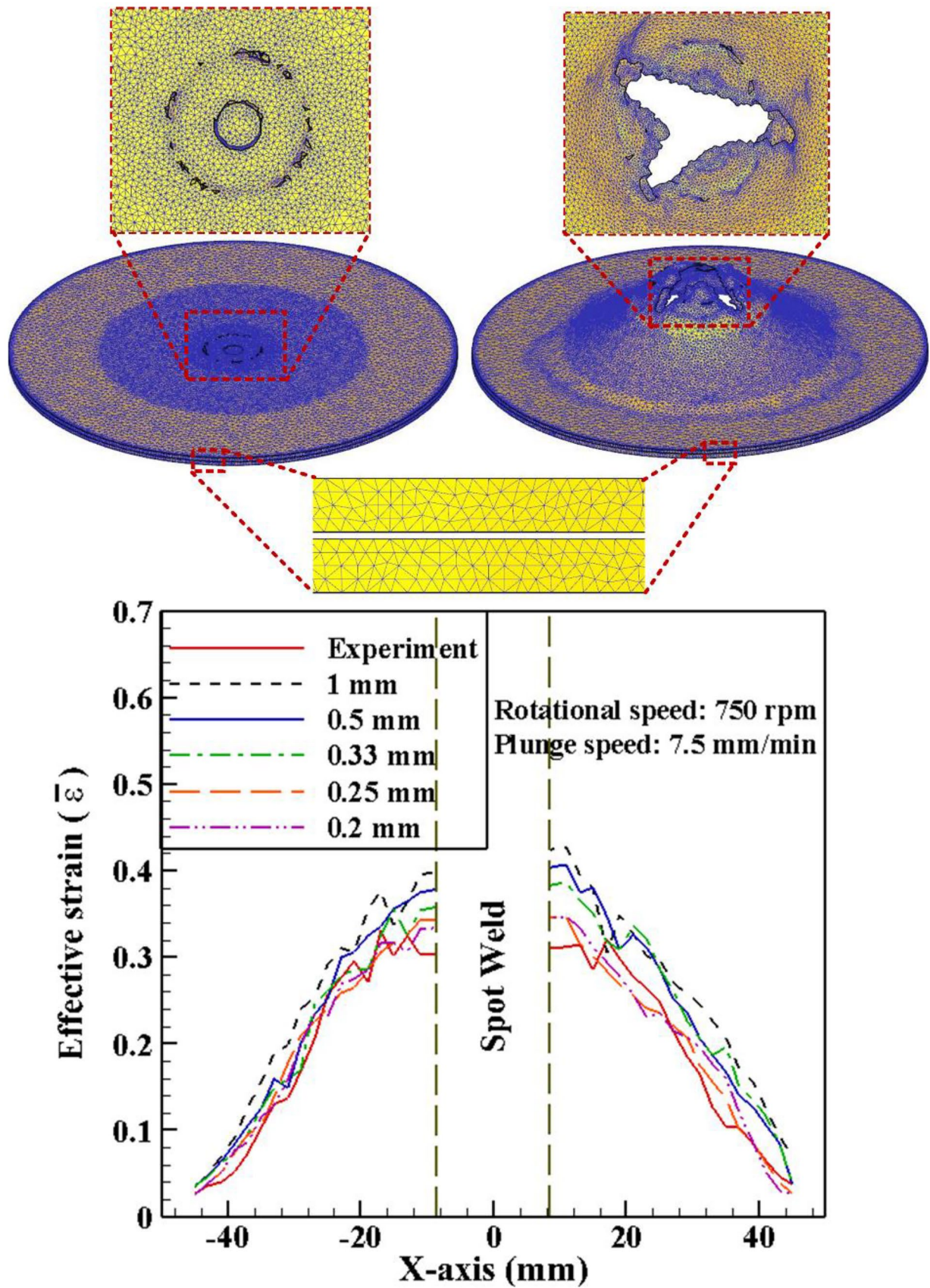
Fig. 11 Comparison of effective strain ($\bar{\varepsilon}$) distribution predicted for different mesh element sizes to experimental data
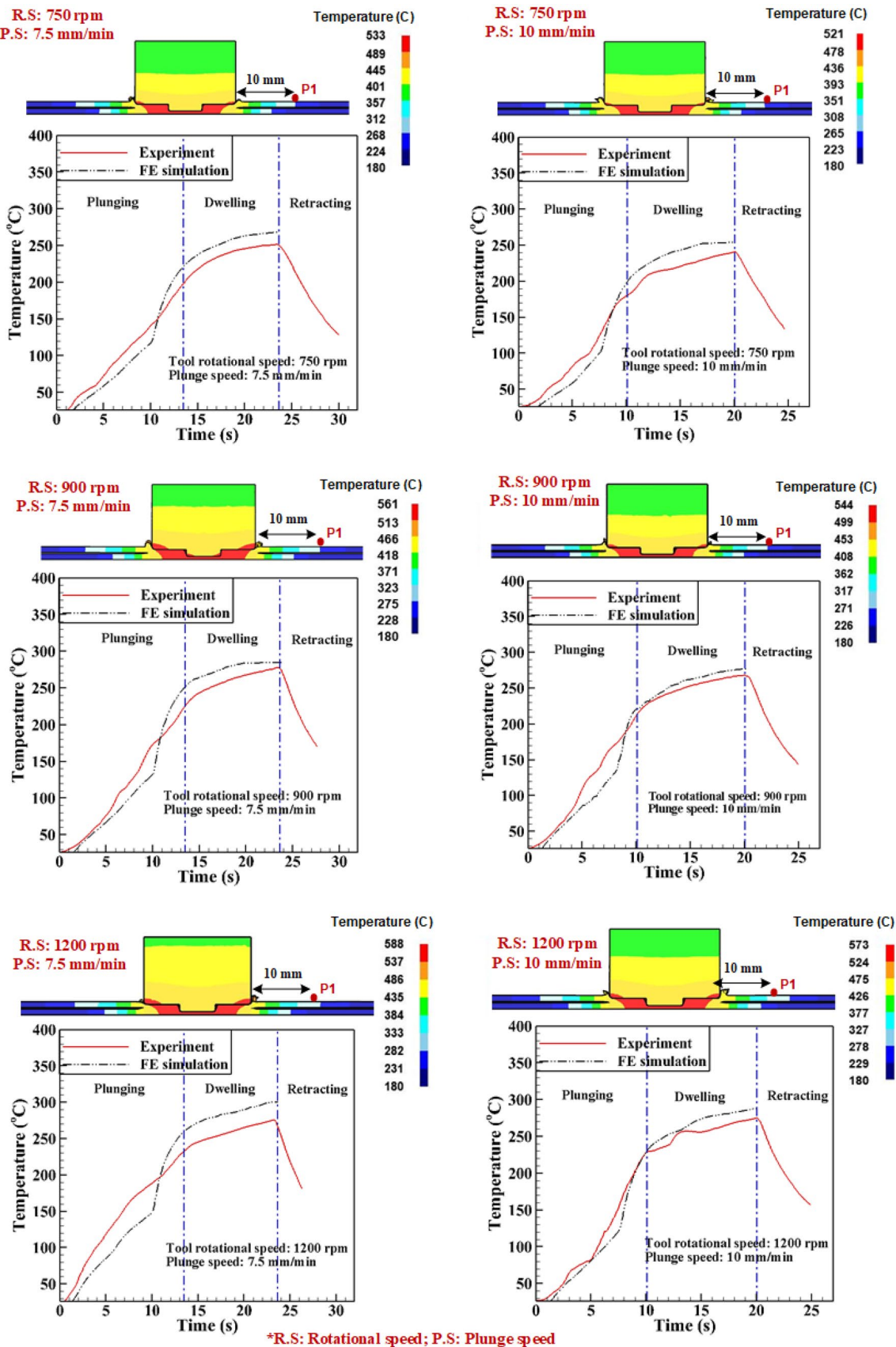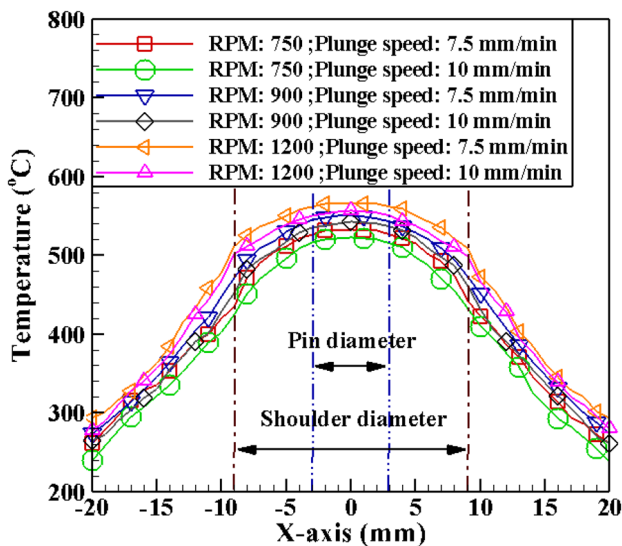
Fig. 12 Comparison of temperature evolution during experiments with that from FE simulations

Fig. 13 Temperature distribution along the transverse section of the spot weld

The shape and size of the stir zone significantly affect the mechanical properties of the joint. During FE simulation of the FSSW, the metallurgical aspect of the material is not considered. Thus, the evolved microstructures during the experiment cannot be compared with FE simulation. However, the point tracking method in DEFORM-3D can be utilized to predict the shape of SZ. During the analysis, total 133 number of points are defined with 0.5 mm horizontal spacing and 0.33 mm vertical spacing on the welded spot (Fig. 14). Due to the symmetry of welding, only half of the weld spot is defined for the purpose. After FSSW, the points are displaced from their initial position because of the plastic deformation caused by the tool. It results in the displacement of points from SZ, and the points away from the SZ remain undisturbed. By connecting line to the position of the border points, SZ can be identified. The results are verified with SZ obtained from the macrostructure (Fig. 14), and a good correlation has been observed. FE simulation results also depict the material deformation mechanism. The position of the points after completion of FSSW clearly elucidates that the material below the center of the tool pin experiences compression, whereas the rest of the material inside SZ experiences both compression and shear deformation (Fig. 14).

FSSW joint morphology can be understood from the macrostructure illustrated in Fig. 15. Badarinarayan et al. [2] reported that out of various characteristics, the combination of larger hook width (horizontal distance from the primary hook to the pinhole periphery) and smaller hook height (vertical distance from the primary hook to hook initiation point) can produce higher joint strength. Thus, in the present study, the effect of rotational speeds and plunge speeds on the hook geometries is quantified (Fig. 15). The hook width increases

significantly with the increase in rotational speed. However, the hook height shows an inverse relation with rotational speed. Bozzi et al. [5] also reported similar observation and indicated that higher rotational speed generates more frictional heat and performs extensive stirring of the material. The severe plastic deformation at higher rotational speed merges a portion of the hook with the extruded material zone, and it results in an increase in bonding width and reduction in hook height. The effect of tool plunge speed is also analyzed, and it is observed that lower plunge speed results in larger hook width. However, the hook height increases with the increase in tool plunge speed. The larger processing time promotes more heat generation and plastic deformation, which leads to increase in the hook width and decrease in hook height.

To visualize the material flow, the point tracking method is utilized during FE simulation of FSSW. Three points, i.e., point 51, point 53, and point 56 (Fig. 14), which are available at the bottom, middle, and top regions of the sheet before the start of the welding are considered. The points are tracked throughout the FSSW operation, and the coordinates of the points are presented in Fig. 16. The choice of assuming single block geometry in the welded section helps to understand the material flow behavior during FSSW without any contact instability. From the results, it is understood that when the rotating tool plunges the upper sheet, the material adjoining to immediately underneath the pin extruded upward (point 56), and it continues until the shoulder contacts the upper surface of the workpiece. Further stirring pushes the material on the upper sheet (point 56) downward and mixes with the middle layer material (point 53). At the same time, the bottom sheet material (point 51) is stirred and lifted upward. The material mixing is more intensive at higher rotational speed, as depicted in Fig. 16. Yang et al. [37] traced the material flow during FSS welding of AZ31 Mg alloy sheets and reported a similar phenomenon for the cause of material mixing during FSSW. The effect of plunge speed on the material mixing during FSSW process is also illustrated in Fig. 16. Larger processing time at lower plunge speed helps in uniform mixing of the material. The increase in plasticization of the material at high temperature expands the bonding region width, as visible in Fig. 15, which leads to the increase in the welding joint strength.

The hardness variation across FSSW at the mid-thickness of the top sheet and bottom sheet is measured (Fig. 17). The hardness in the periphery of the pinhole is maximum because of the finer grains in SZ (Fig. 14). On the other hand, the hardness across the periphery of the shoulder is lower on the top sheet. A slight decrement in hardness is also visible below the shoulder region in the bottom sheet. The localized decrement in the hardness is because of the softening of the material due to metallurgical recovery after the thermal cycle [9]. The intensive stirring of the material at the higher rotational speed leads to dynamic recrystallization, and it results in an increase in hardness. Huskins
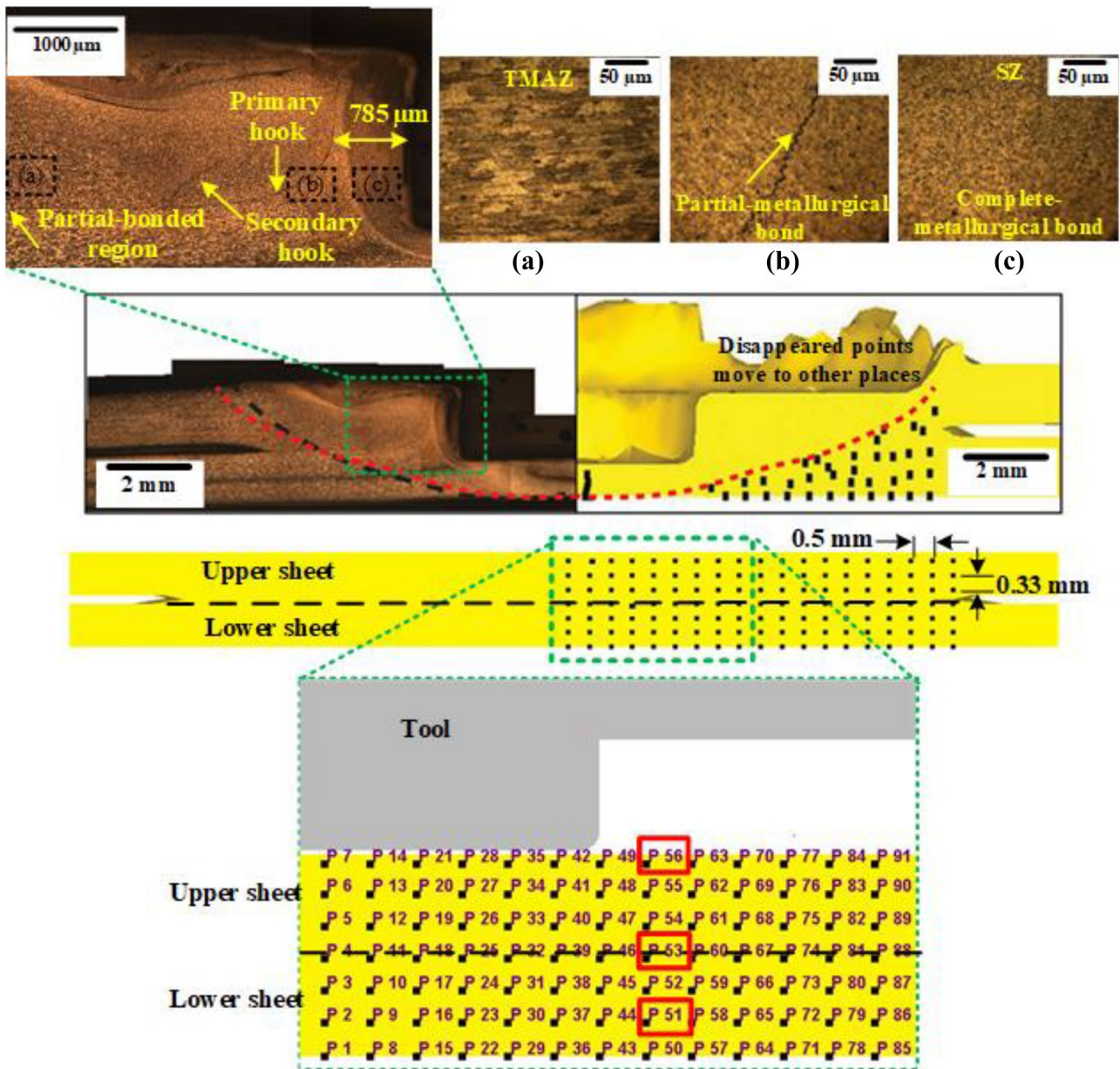
Fig. 14 (**a**) Characterization of the weld spot for welding condition, tool rotational speed: 750 rpm, plunge speed: 7.5 mm/min, and (**b**) Measurement of SZ size and comparison with FE simulation

et al. [38] reported that apart from grain boundary strengthening, precipitation hardening and increase in dislocation density at the higher rotational speed increase the hardness of AA 5XXX alloys during FSW process. Though the material mixing is uniform at lower plunge speed (Fig. 16), its effect is less significant in hardness variation.

4.3 Deformation profile prediction

The sheets with FS spot welds are deformed at high strain rate until fracture in a shock tube and the same phenomenon has been modeled using FE simulation. All the FSSW sheets are deformed at a striker velocity of 68.55 m/s, and the final height of deformation is defined as the stopping control for the simulation. The final height is the height observed in shock tube-based forming experiments. The deformation profiles predicted by MJC model in combination with the Freudenthal damage model are compared with the experiment, and a good correlation is observed (Fig. 18). The final height of deformation is strongly dependent on the weld strength. Larger hook width and increase in hardness in the welded joint
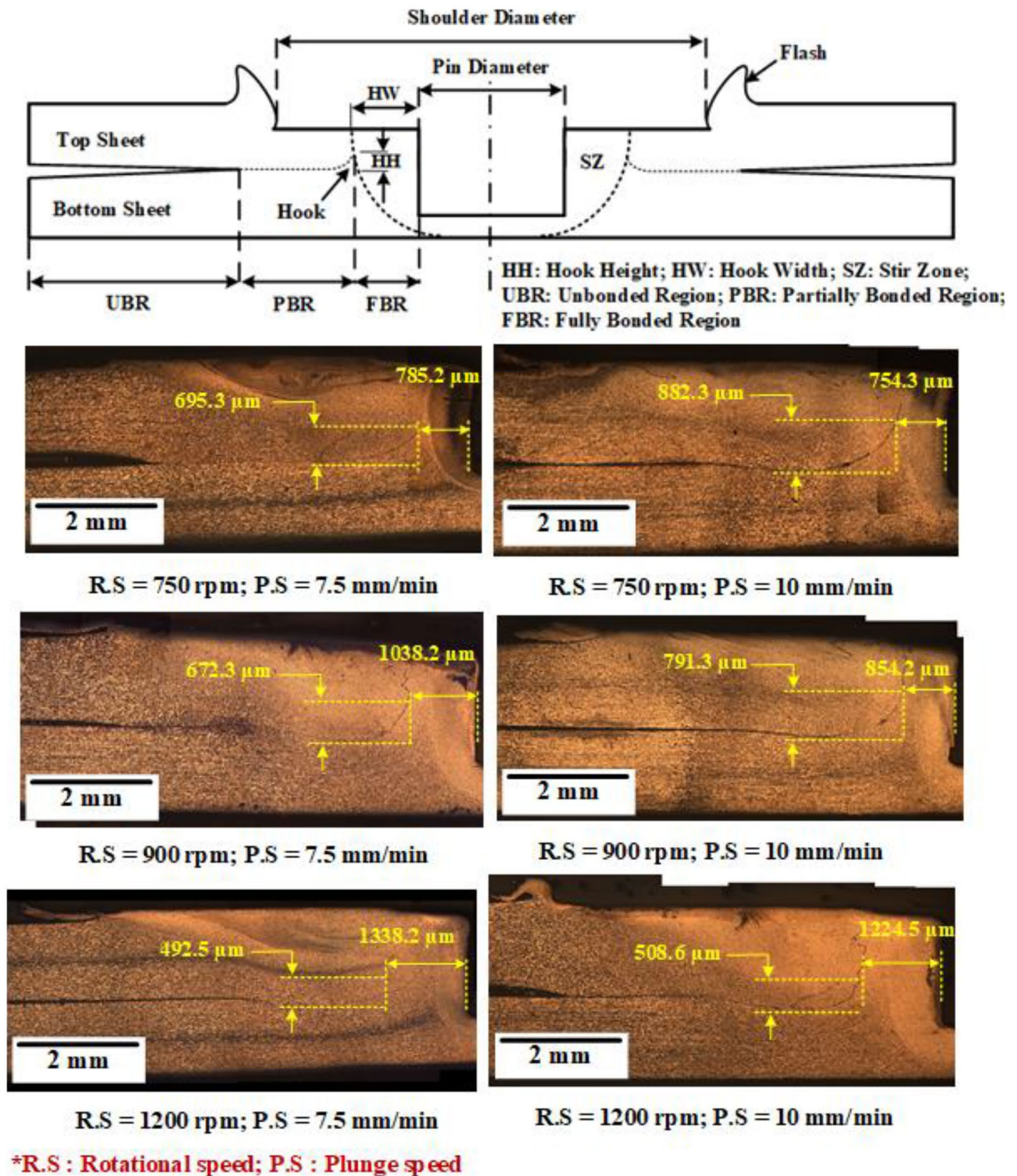
Fig. 15 Hook morphology of the welded joints at different welding conditions

clearly indicate the rise in welding strength [2, 9]. Its effect can be directly related to the final height of deformation. FSSW sheet made at 900 rpm has lower height of deformation than 750 rpm case. In both the cases, failure starts from the welded region. On the other hand, in 1200 rpm, the sheet fails outside the welded region, in the base material. The detailed failure behavior of the welded sheets is described in Sect. 4.5.
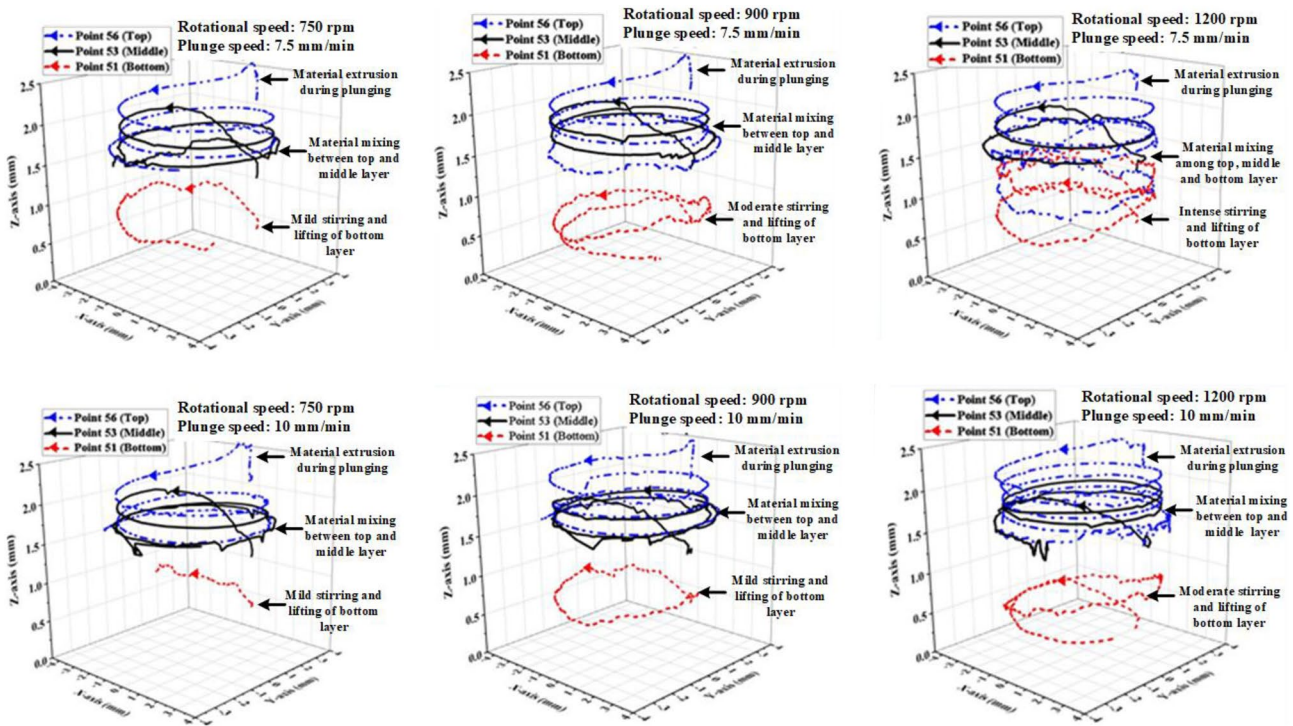
Fig. 16 Material flow visualization at different FSSW cases

4.4 Prediction of necking height

During high-velocity forming in the shock tube, it is difficult to capture the necking phenomenon experimentally. Thus, the dome height at necking is predicted from FE simulation. Circular grid flow pattern is generated on the surface of the sheet before the start of the forming simulation (Fig. 10a). When the damage value reaches the critical limit, necking initiates. The dome height at the onset of necking is obtained from FE simulation and elucidated
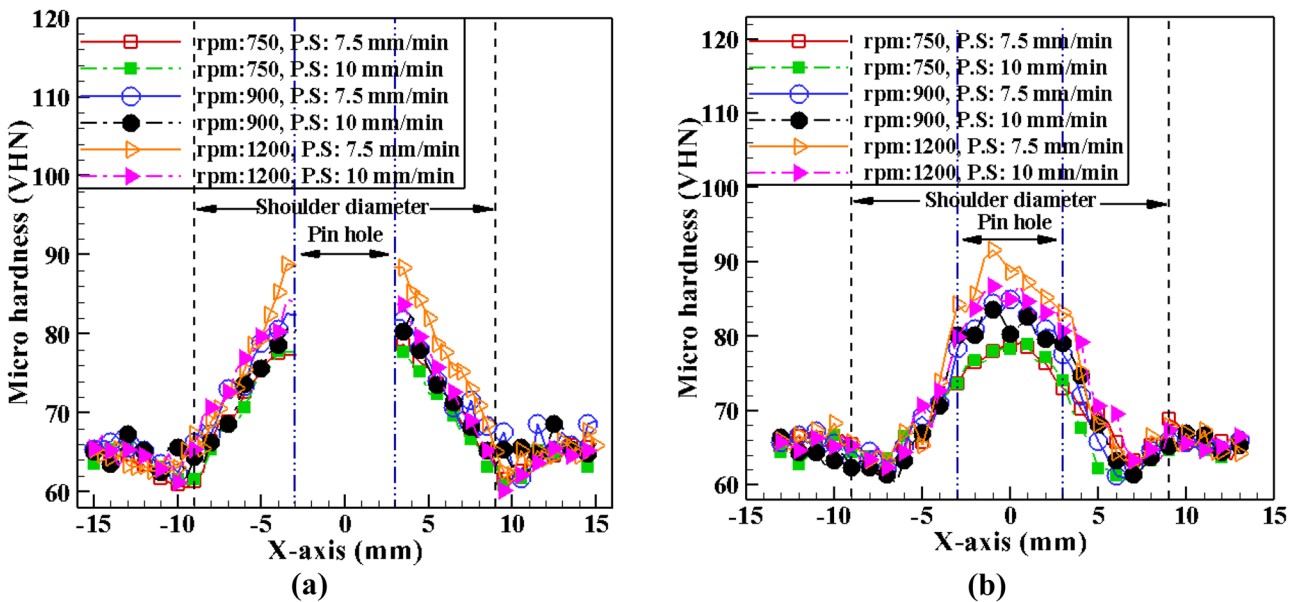
Fig. 17 Hardness distribution at the mid thickness of **a** top sheet and **b** bottom sheet. *rpm: rotation per minute; P.S: plunge speed
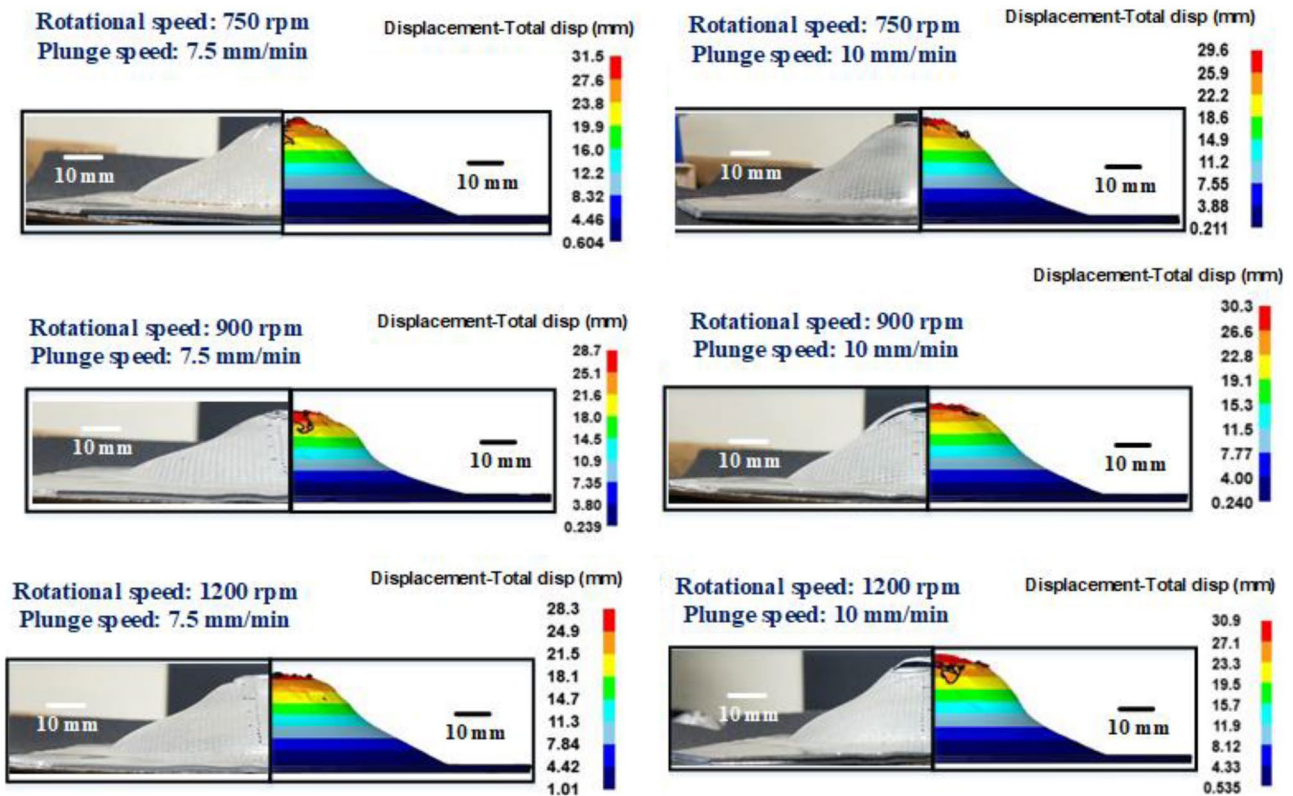
Fig. 18 Prediction of the deformation profile of the FSSW sheet

in Fig. 19. For all the welded sheets, necking initiates from the pinhole. However, the welding strength significantly affects the dome height at necking. FSSW sheet made at 1200 rpm starts necking at larger height than 750 rpm and 900 rpm weld cases. However, the effect of plunge speed on the height at necking is insignificant.

Fig. 19 Prediction of dome height at necking of sheets with FSSW
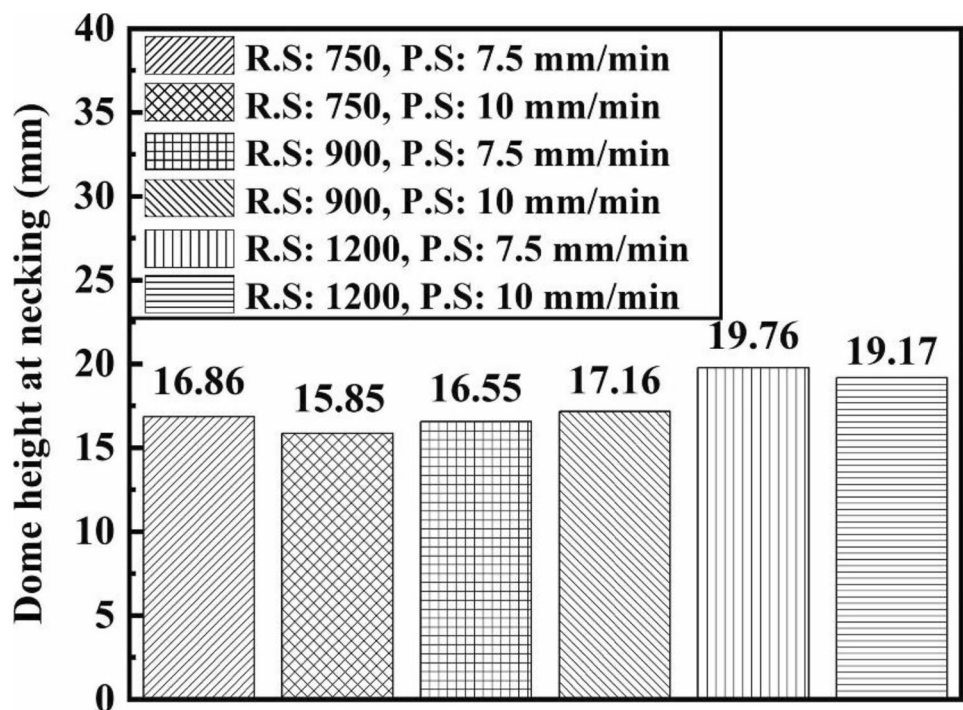
4.5 Effective strain distribution and failure pattern

During forming experiments, all the FSSW sheets fail after deformation. However, the changes in crack pattern, crack propagation length, and height of deformation directly depend on the weld strength. The predicted crack pattern developed on the welded sheets after reaching the final height of deformation matches quite well with the experimental data (Fig. 20). The results elucidate that the necking initiates from the pinhole. However, the increase in weld strength at 1200 rpm restricts the further propagation of the crack, and the sheets fail from the base material (Fig. 20).

For the other two rotational speeds, 750 rpm and 900 rpm, the crack initiates and propagates from the pinhole. The variation in tool plunge speed does not affect the crack pattern on the FSSW sheets significantly (Fig. 20). However, lower crack propagation length (confirmed by visual inspection in Fig. 20) and dome height (Fig. 18) of the FSSW sheets generated at lower plunge speed directly signifies the increase in weld strength.

Effective strain distribution predicted during FE simulation is also compared with the experimental results, and an acceptable correlation has been observed (Fig. 21). The effective strain developed on the welded sheets during
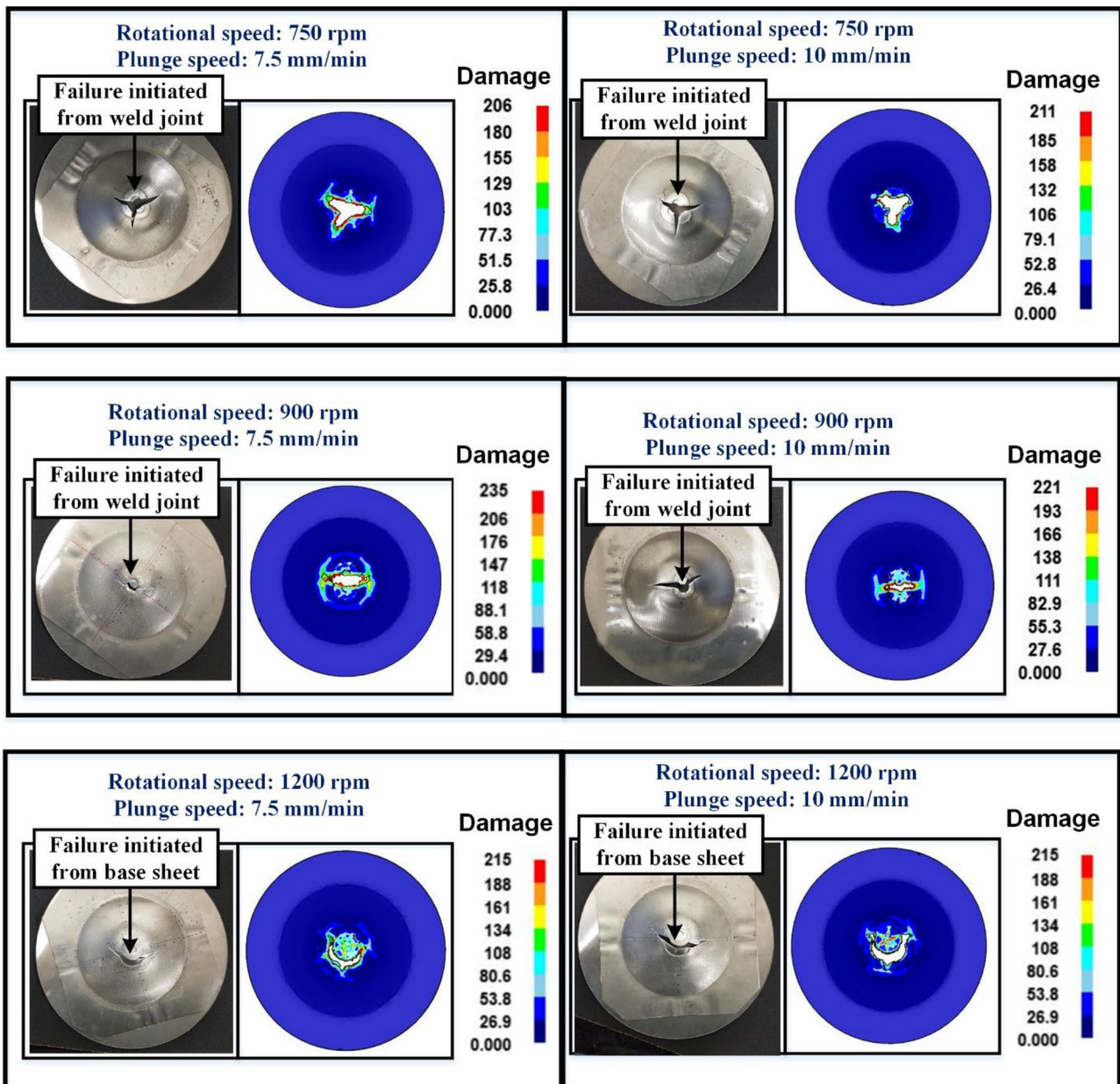

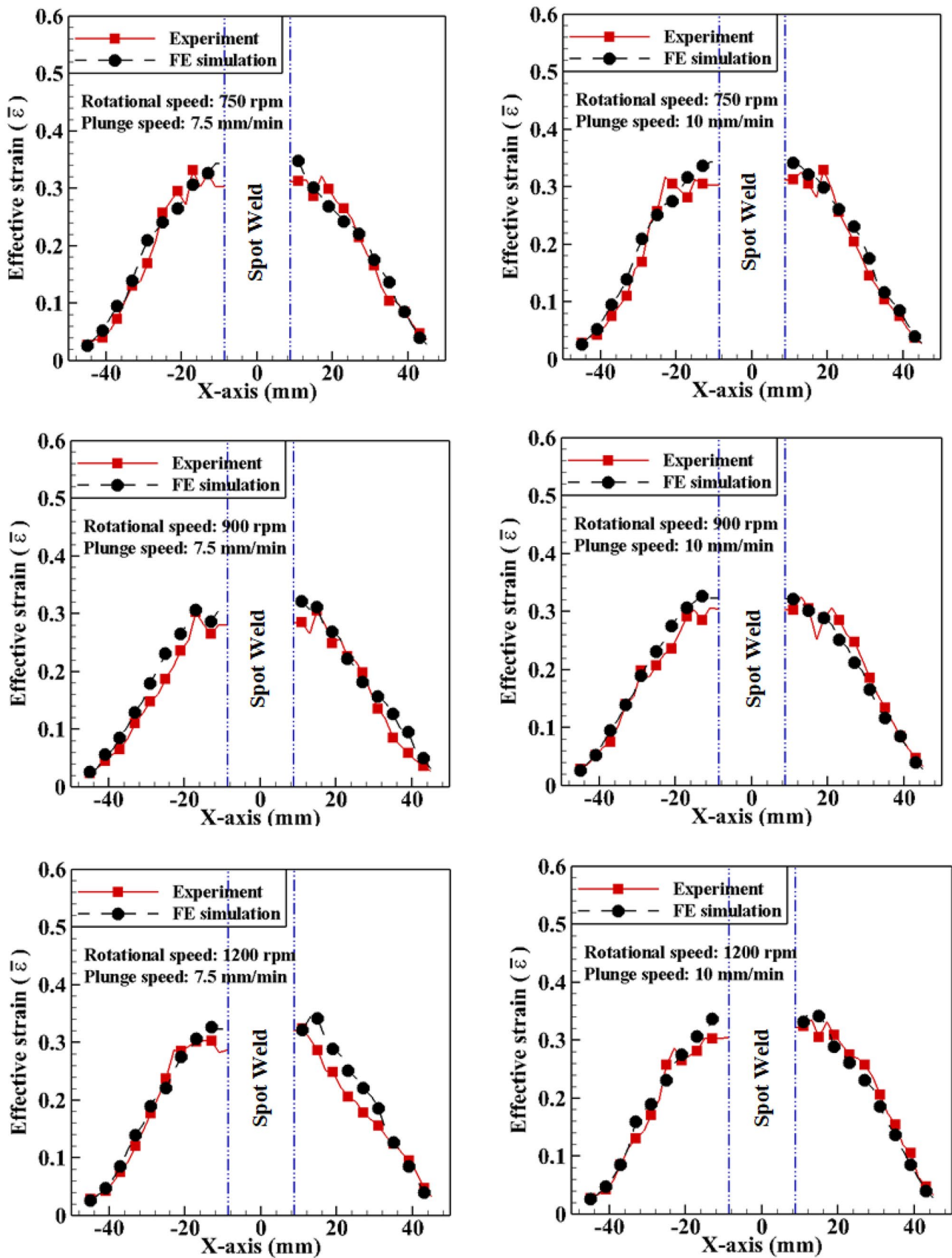**Fig. 20** Failure pattern prediction and comparison with experimental observation

Fig. 21 Comparison of predicted effective strain with experimental data for FSSW sheets

forming confirms the uniform stretching of the material. The inertial effect developed during this dynamic forming environment restricts the strain localization in the material, which helps to increase in formability of the deformed sheet [26]. The results ensure the better predictability of the Freudenthal damage model in combination with the MJC model for all the welded sheets.

5 Conclusions

The present work aims to understand the formability of AA 5052-H32 sheets with friction stir spot welds at high strain rates. Forming is performed using a shock tube. Effect of tool rotational speed and plunge speed on the FSSW outputs and forming outputs is evaluated. Numerical simulations of FSSW and forming with FSS welds are carried out at experimental conditions using DEFORM-3D to understand the rate-dependent formability. The following conclusions are drawn from the results.

(i) A two-stage manufacturing process constituting FSSW of sheet as first stage and impact forming as second stage has been implemented at lab scale, and the same has been predicted by FE simulations. The overall results are encouraging. Through this work, a validated experimental-modelling strategy has been presented to design the two-stage manufacturing process.

(ii) During FE simulation of impact forming, the rate-dependent flow stress–strain data for the unwelded section of the FSSW sheet are identified from the tensile test of the sheet deformed by shock tube, and for the spot weld region, a hardness multiplying factor is identified for the purpose. The approaches are simple to implement in laboratory and sufficiently accurate in predicting the formability of sheets with spot welds.

(iii) The temperature evolution during FSSW clearly signifies that the temperature rise is directly proportional to the tool rotational speed. However, the rate of temperature rise with the increase in plunge speed is insignificant.

(iv) The material flow visualization during FSSW elucidates the intensive material mixing phenomenon at higher rotational speed. Furthermore, larger processing time at lower plunge speed promotes more uniform plastic deformation that leads to an increase in bonding width.

(v) Larger weld strength at higher rotational speed delays the necking phenomenon during forming of FSSW sheet. It results in larger dome height at necking. Though necking initiates from the pinhole for all the weld cases, increase in strength at 1200 rpm restricts

further crack propagation, and the sheet fails from the base material. Same phenomenon is also captured during FE simulation. The variation of tool plunge speed has insignificant effect on the dome height and the failure pattern.

(vi) FSSW joint morphology confirms that the hook width increases significantly with the increase in the tool rotational speed. However, the hook height shows an inverse relation with the rotational speed. At the same time, lower plunge speed results in larger hook width and smaller hook height because of larger heat generation and plastic deformation

(vii) Deformation profile, failure pattern, and effective strain distribution predicted by MJC flow stress model in combination with Freudenthal damage model have a fair agreement with the experimental results.

Author contribution Saibal Kanchan Barik conceived and designed the study, performed the experiments and numerical simulations, performed the analysis, and wrote the paper. R. Ganesh Narayanan conceived and designed the study, and contributed to the analysis, final proof reading. Niranjan Sahoo conceived and designed the study, and contributed to the analysis, final proof reading.

Availability of data and material We confirm that data is open and transparent.

Declarations

Ethics approval Not applicable.

Consent to participate Not applicable.

Consent for publication Not applicable.

Competing interests The authors declare no competing interests.

Appendix: Identification of stress ratio and strain ratio for plane strain condition with no planar anisotropy

Hill's 1948 yield criterion for anisotropic materials in principal coordinate system is expressed as [39]:

$$F(\sigma_2 - \sigma_3)^2 + G(\sigma_3 - \sigma_1)^2 + H(\sigma_1 - \sigma_2)^2 = \frac{2}{3}(F + G + H)\bar{\sigma}^2 \tag{9}$$

where F, G, and H are the anisotropy parameters; σ_i represents the principal stress.

During plastic deformation, the stress and the strain are related by the flow rule,

$$d\varepsilon_{ij} = d\lambda \frac{\partial f(\sigma_{ij})}{\partial \sigma_{ij}} \qquad (10)$$

where $d\lambda$ is an arbitrary constant.

The principal strains ($d\varepsilon_1, d\varepsilon_2, d\varepsilon_3$) for plane stress condition can be obtained by differentiating Eq. (10) with respect to the principal stresses and substituting into the flow rule.

$$\begin{aligned}
d\varepsilon_1 &= d\lambda\left[G(\sigma_1 - \sigma_3) + H(\sigma_1 - \sigma_2)\right] \\
d\varepsilon_2 &= d\lambda\left[F(\sigma_2 - \sigma_3) + H(\sigma_2 - \sigma_1)\right] \\
d\varepsilon_3 &= d\lambda\left[G(\sigma_3 - \sigma_1) + F(\sigma_3 - \sigma_2)\right]
\end{aligned} \qquad (11)$$

Assuming plane stress condition for thin sheet, Hill's 1948 yield criterion can be demonstrated as:

$$F(\sigma_2)^2 + G(\sigma_1)^2 + H(\sigma_1 - \sigma_2)^2 = \frac{2}{3}(F + G + H)\bar{\sigma}^2 \qquad (12)$$

By substituting principal stress ratio, $\alpha = \sigma_2/\sigma_1$ into Eq. (12)

$$F(\alpha)^2 + G + H(1 - \alpha)^2 = \frac{2}{3}(F + G + H)\frac{\bar{\sigma}^2}{\sigma_1^2} \qquad (13)$$

The principal strain ratio, $\beta = d\varepsilon_2/d\varepsilon_1$ for plane stress condition, can be expressed as:

$$\beta = \frac{F(\alpha) - H(1 - \alpha)}{G + H(1 - \alpha)} \qquad (14)$$

Assuming plane strain condition ($\beta = 0$), α will be expressed as:

$$\alpha = \frac{H}{F + H} \qquad (15)$$

For no planar anisotropy condition ($r = r_0 = r_{45} = r_{90}$), Hill's anisotropic constants (F, G, and H) can be correlated as $F = G$ and $H = rG$.

Substituting F, G, and H into Eq. (12), the stress ratio can be obtained as:

$$\frac{\sigma_1}{\bar{\sigma}} = \sqrt{\frac{2(2 + r)(1 + r)}{3(1 + 2r)}} \qquad (16)$$

The principle of equivalent plastic work for plane stress condition is defined as:

$$\bar{\sigma}d\bar{\varepsilon} = \sigma_1 d\varepsilon_1 + \sigma_2 d\varepsilon_2 \qquad (17)$$

The $d\bar{\varepsilon}/d\varepsilon_1$ can be derived as:

$$\frac{d\bar{\varepsilon}}{d\varepsilon_1} = \sqrt{\frac{2(2 + r)(1 + r)}{3(1 + 2r)}} \qquad (18)$$

References

1. Çam G, İpekoğlu G (2017) Recent developments in joining of aluminum alloys. Int J Adv Manuf Technol 91:1851–1866. https://doi.org/10.1007/s00170-016-9861-0

2. Badarinarayan H, Shi Y, Li X, Okamoto K (2009) Effect of tool geometry on hook formation and static strength of friction stir spot welded aluminum 5754-O sheets. Int J Mach Tools Manuf 49:814–823. https://doi.org/10.1016/j.ijmachtools.2009.06.001

3. Karthikeyan R, Balasubramanian V (2010) Predictions of the optimized friction stir spot welding process parameters for joining AA2024 aluminum alloy using RSM. Int J Adv Manuf Technol 51:173–183. https://doi.org/10.1007/s00170-010-2618-2

4. Babu S, Sankar VS, Ram GDJ et al (2013) Microstructures and mechanical properties of friction stir spot welded aluminum alloy AA2014. J Mater Eng Perform 22:71–84. https://doi.org/10.1007/s11665-012-0218-z

5. Bozzi S, Helbert-Etter AL, Baudin T et al (2010) Influence of FSSW parameters on fracture mechanisms of 5182 aluminium welds. J Mater Process Technol 210:1429–1435. https://doi.org/10.1016/j.jmatprotec.2010.03.022

6. Yuan W, Mishra RS, Carlson B et al (2012) Material flow and microstructural evolution during friction stir spot welding of AZ31 magnesium alloy. Mater Sci Eng A 543:200–209. https://doi.org/10.1016/j.msea.2012.02.075

7. Ji S, Wang Y, Zhang J, Li Z (2017) Influence of rotating speed on microstructure and peel strength of friction spot welded 2024–T4 aluminum alloy. Int J Adv Manuf Technol 90:717–723. https://doi.org/10.1007/s00170-016-9398-2

8. Tozaki Y, Uematsu Y, Tokaji K (2007) Effect of processing parameters on static strength of dissimilar friction stir spot welds between different aluminium alloys. Fatigue Fract Eng Mater Struct 30:143–148. https://doi.org/10.1111/j.1460-2695.2006.01096.x

9. Rana PK, Narayanan RG, Kailas SV (2018) Effect of rotational speed on friction stir spot welding of AA5052-H32/HDPE/AA5052-H32 sandwich sheets. J Mater Process Technol 252:511–523. https://doi.org/10.1016/j.jmatprotec.2017.10.016

10. Noh W, Koh Y, Chung K et al (2018) Influence of dynamic loading on failure behavior of spot welded automotive steel sheets. Int J Mech Sci 144:407–426. https://doi.org/10.1016/j.ijmecsci.2018.06.009

11. Kesharwani RK, Basak S, Panda SK, Pal SK (2017) Improvement in limiting drawing ratio of aluminum tailored friction stir welded blanks using modified conical tractrix die. J Manuf Process 28:137–155. https://doi.org/10.1016/j.jmapro.2017.06.002

12. Ramulu PJ, Narayanan RG, Kailas SV (2013) Forming limit investigation of friction stir welded sheets: influence of shoulder diameter and plunge depth. Int J Adv Manuf Technol 69:2757–2772. https://doi.org/10.1007/s00170-013-5245-x

13. Kim D, Lee W, Kim J et al (2010) Formability evaluation of friction stir welded 6111–T4 sheet with respect to joining material direction. Int J Mech Sci 52:612–625. https://doi.org/10.1016/j.ijmecsci.2010.01.001

14. Parente M, Safdarian R, Santos AD et al (2016) A study on the formability of aluminum tailor welded blanks produced by friction stir welding. Int J Adv Manuf Technol 83:2129–2141. https://doi.org/10.1007/s00170-015-7950-0

15. Kim D, Lee W, Kim J et al (2010) Macro-performance evaluation of friction stir welded automotive tailor-welded blank sheets: Part II–Formability. Int J Solids Struct 47:1063–1081. https://doi.org/10.1016/j.ijsolstr.2009.12.021

16. Habibi M, Hashemi R, Tafti MF, Assempour A (2018) Experimental investigation of mechanical properties, formability and forming limit diagrams for tailor-welded blanks produced by

friction stir welding. J Manuf Process 31:310–323. https://doi.org/10.1016/j.ijsolstr.2009.12.021

17. Feng F, Li J, Huang L et al (2021) Formability enhancement of 5052 aluminium alloy sheet in electromagnetic impaction forming. Int J Adv Manuf Technol 112:2639–2655. https://doi.org/10.1007/s00170-020-06483-4

18. Sun X, Khaleel MA (2007) Dynamic strength evaluations for self-piercing rivets and resistance spot welds joining similar and dissimilar metals. Int J Impact Eng 34:1668–1682. https://doi.org/10.1016/j.ijimpeng.2006.09.092

19. Ambriz RR, Froustey C, Mesmacque G (2013) Determination of the tensile behavior at middle strain rate of AA6061-T6 aluminum alloy welds. Int J Impact Eng 60:107–119. https://doi.org/10.1016/S1003-6326(20)65239-6

20. Barik SK, Narayanan RG, Sahoo N (2020) Forming response of AA5052–H32 sheet deformed using a shock tube. Trans Nonferrous Met Soc China 30:603–618. https://doi.org/10.1016/S1003-6326(20)65239-6

21. Stoffel M, Schmidt R, Weichert D (2001) Shock wave-loaded plates. Int J Solids Struct 38:7659–7680. https://doi.org/10.1016/S0020-7683(01)00038-5

22. Justusson B, Pankow M, Heinrich C et al (2013) Use of a shock tube to determine the bi-axial yield of an aluminum alloy under high rates. Int J Impact Eng 58:55–65. https://doi.org/10.1016/j.ijimpeng.2013.01.012

23. Chen D-Y, Xu Y, Zhang S-H et al (2021) A novel method to evaluate the high strain rate formability of sheet metals under impact hydroforming. J Mater Process Technol 287:116553. https://doi.org/10.1016/j.jmatprotec.2019.116553

24. Barik SK, Narayanan RG, Sahoo N (2020) Prediction of forming of AA 5052–H32 sheets under impact loading and experimental validation. J Mater Eng Perform 29:3941–3960. https://doi.org/10.1007/s11665-020-04884-w

25. Ray N, Jagadeesh G, Suwas S (2015) Response of shock wave deformation in AA5086 aluminum alloy. Mater Sci Eng A 622:219–227. https://doi.org/10.1016/j.msea.2014.10.010

26. Barik SK, Narayanan GR, Sahoo N (2021) Failure strain and fracture prediction during shock tube impact forming of AA 5052–H32 sheet. J Eng Mater Technol 143:031009. https://doi.org/10.1115/1.4050703

27. Zhang Z, Yang X, Zhang J et al (2011) Effect of welding parameters on microstructure and mechanical properties of friction stir spot welded 5052 aluminum alloy. Mater Des 32:4461–4470. https://doi.org/10.1016/j.matdes.2011.03.058.

28. Barik SK, Narayanan RG, Sahoo N (2019) Experimental investigation on the forming of AA 5052-H32 sheet using a rigid-body-based impact in a shock tube. In: Advances in Forming, Machining and Automation. Springer, pp 79–90. https://doi.org/10.1007/978-981-32-9417-2_6.

29. Zhao Y, Liu H, Yang T et al (2016) Study of temperature and material flow during friction spot welding of 7B04-T74 aluminum alloy. Int J Adv Manuf Technol 83:1467–1475. https://doi.org/10.1007/s00170-015-7681-2

30. Bajpei T, Chelladurai H, Ansari MZ (2017) Experimental investigation and numerical analyses of residual stresses and distortions in GMA welding of thin dissimilar AA5052-AA6061 plates. J Manuf Process 25:340–350. https://doi.org/10.1016/j.jmapro.2016.12.017

31. Fluhrer J (2007) DEFORM 3D Version 6.1 User's Manual. Sci Form Technol Corp Ohio

32. Song P, Li W, Wang X, Xu W (2019) Study on mechanical properties and constitutive model of 5052 aluminium alloy. Mater Sci Technol 35:916–924. https://doi.org/10.1016/j.jmapro.2016.12.017

33. Khodko O, Zaytsev V, Sukaylo V et al (2015) Experimental and numerical investigation of processes that occur during high velocity hydroforming technologies: an example of tubular blank free bulging during hydrodynamic forming. J Manuf Process 20:304–313. https://doi.org/10.1016/j.jmapro.2015.06.016

34. Deng H, Mao Y, Li G, Cui J (2019) A study of electromagnetic free forming in AA5052 using digital image correlation method and FE analysis. J Manuf Process 37:595–605. https://doi.org/10.1016/j.jmapro.2018.12.033

35. Wagoner RH, Chenot J-L (1996) Fundamentals of metal forming. John Wiley & Sons Inc, New York

36. Buffa G, Hua J, Shivpuri R, Fratini L (2006) A continuum based fem model for friction stir welding—model development. Mater Sci Eng A 419:389–396. https://doi.org/10.1016/j.msea.2005.09.040

37. Yang Q, Mironov S, Sato YS, Okamoto K (2010) Material flow during friction stir spot welding. Mater Sci Eng A 527:4389–4398. https://doi.org/10.1016/j.msea.2010.03.082

38. Huskins EL, Cao B, Ramesh KT (2010) Strengthening mechanisms in an Al-Mg alloy. Mater Sci Eng A 527:1292–1298. https://doi.org/10.1016/j.msea.2009.11.056

39. Takuda H, Mori K, Hatta N (1999) The application of some criteria for ductile fracture to the prediction of the forming limit of sheet metals. J Mater Process Technol 95:116–121. https://doi.org/10.1016/S0924-0136(99)00275-7